NEUROSCIENCE

Presynaptic nanoscale components of retrograde synaptic signaling

Benjámin Barti[1,2,3], Barna Dudok[2,4,5], Kata Kenesei[2], Miklós Zöldi[1,2,3], Vivien Miczán[2,6], Gyula Y. Balla[2,3,7], Diana Zala[8], Mariana Tasso[9], Claudia Sagheddu[10], Máté Kisfali[2,11], Blanka Tóth[12,13], Marco Ledri[2,14], E. Sylvester Vizi[15], Miriam Melis[10], László Barna[1], Zsolt Lenkei[8], Iván Soltész[5], István Katona[1,2]*

While our understanding of the nanoscale architecture of anterograde synaptic transmission is rapidly expanding, the qualitative and quantitative molecular principles underlying distinct mechanisms of retrograde synaptic communication remain elusive. We show that a particular form of tonic cannabinoid signaling is essential for setting target cell–dependent synaptic variability. It does not require the activity of the two major endocannabinoid-producing enzymes. Instead, by developing a workflow for physiological, anatomical, and molecular measurements at the same unitary synapse, we demonstrate that the nanoscale stoichiometric ratio of type 1 cannabinoid receptors (CB_1Rs) to the release machinery is sufficient to predict synapse-specific release probability. Accordingly, selective decrease of extrasynaptic CB_1Rs does not affect synaptic transmission, whereas in vivo exposure to the phytocannabinoid Δ^9-tetrahydrocannabinol disrupts the intrasynaptic nanoscale stoichiometry and reduces synaptic variability. These findings imply that synapses leverage the nanoscale stoichiometry of presynaptic receptor coupling to the release machinery to establish synaptic strength in a target cell–dependent manner.

INTRODUCTION

Input-output transformation in neurons is regulated by the strength of synaptic connections. Recent innovations in super-resolution microscopy helped to determine how the strength of anterograde synaptic transmission is determined by quantitative properties of the subsynaptic topography of molecular machineries (*1*, *2*). The precise nanoscale alignment of the presynaptic release machinery with postsynaptic receptor clusters and the activity-dependent assembly of these trans-synaptic nanomodules are essential molecular determinants of glutamatergic and γ-aminobutyric acid (GABA)–releasing (GABAergic) synaptic transmission (*3*–*6*). Local feedback regulatory mechanisms also play important roles in adjusting synaptic strength (*7*). For example, endocannabinoids are ubiquitous retrograde messengers mediating synaptic plasticity via activation of presynaptic type 1 cannabinoid receptors (CB_1Rs) (*8*). Notably, CB_1R is one of the most enriched transmembrane proteins in neurons, with levels comparable to major postsynaptic receptors such as α-amino-3-hydroxy-5-methyl-4-isoxazolepropionic acid (AMPA), *N*-methyl-D-aspartate, and γ-aminobutyric acid type A ($GABA_A$) (*9*). Yet, in contrast to the nanoscale architecture that governs anterograde synaptic transmission via postsynaptic receptors, the nanoscale functional organization that determines how retrograde synaptic signaling and presynaptic CB_1Rs control neurotransmitter release remains poorly understood.

Distinct forms of CB_1R-dependent retrograde cannabinoid signaling regulate synaptic transmission at different temporal scales. A so-called tonic form requires intact neuroligin-3 function and calcium signaling in the postsynaptic neuron, but it is expressed as persistent presynaptic inhibition of neurotransmitter release (*10*–*12*). Tonic cannabinoid signaling, but not other forms of endocannabinoid-mediated synaptic plasticity, is selectively disrupted in mouse models of autism. This highlights its specific pathological relevance and postulates that mechanistically diverse processes underlie different types of retrograde cannabinoid signaling (*12*, *13*).

Anandamide (AEA) and 2-arachidonoylglycerol (2-AG) are the two major endocannabinoid messengers (*14*). There is broad consensus that the so-called phasic forms of endocannabinoid-mediated synaptic plasticity require on-demand synthesis of 2-AG by the diacylglycerol lipase-α (DAGLα) enzyme (*15*). In contrast, the mechanistic attributes of tonic cannabinoid signaling remain debated. On the basis of the use of enzyme inhibitors, both AEA and 2-AG have been proposed to be the primary endocannabinoid messenger in tonic endocannabinoid signaling in ex vivo and in vivo experimental models leading to lasting dampening of neurotransmitter release (*16*–*20*). Moreover, the role of CB_1Rs in tonic endocannabinoid signaling, which is measured by the use of CB_1R antagonists/inverse agonists, has also been questioned because of the off-target effects of these pharmacological tools on several synaptic receptors (*21*–*24*). Thus, more selective genetic approaches are required to elucidate the signaling mechanism and the nanoscale functional organization that underlies the synaptic cannabinoid tone.

[1]Department of Psychological and Brain Sciences, Indiana University Bloomington, 702 N Walnut Grove Ave, Bloomington, IN 47405-2204, USA. [2]Molecular Neurobiology Research Group, HUN-REN Institute of Experimental Medicine, Szigony st 43, H-1083 Budapest, Hungary. [3]School of Ph.D. Studies, Semmelweis University, Üllői st 26, H-1085 Budapest, Hungary. [4]Departments of Neurology and Neuroscience, Baylor College of Medicine, 1 Baylor Plz, Houston, TX 77030, USA. [5]Department of Neurosurgery, Stanford University, 450 Jane Stanford Way, Stanford, CA 94305, USA. [6]Synthetic and Systems Biology Unit, HUN-REN Biological Research Center, Temesvári krt. 62, H-6726 Szeged, Hungary. [7]Translational Behavioral Neuroscience Research Group, HUN-REN Institute of Experimental Medicine, Szigony st 43, H-1083 Budapest, Hungary. [8]Université Paris Cité, INSERM, Institute of Psychiatry and Neurosciences of Paris, F-75014 Paris, France. [9]Institute of Nanosystems, School of Bio and Nanotechnologies, National University of San Martín - CONICET, 25 de Mayo Ave., 1021 San Martín, Argentina. [10]Department of Biomedical Sciences, University of Cagliari, Cittadella Universitaria di Monserrato, Monserrato, 09042 Cagliari, Italy. [11]BiTrial Ltd., Tállya st 23, H-1121 Budapest, Hungary. [12]Department of Inorganic and Analytical Chemistry, Budapest University of Technology and Economics, Szt. Gellért square 4, H-1111 Budapest, Hungary. [13]Department of Molecular Biology, Semmelweis University, Üllői st 26, H-1085 Budapest, Hungary. [14]Epilepsy Center, Department of Clinical Sciences, Faculty of Medicine, Lund University, Sölvegatan 17, BMC A11, 221 84 Lund, Sweden. [15]Molecular Pharmacology Research Group, HUN-REN Institute of Experimental Medicine, Szigony st 43, H-1083 Budapest, Hungary.
*Corresponding author. Email: ikatona@iu.edu, katona@koki.hu

An interesting feature of tonic cannabinoid signaling is its synapse specificity in brain circuits (*25*–*27*). For example, persistent CB_1R activity selectively regulates perisomatically targeting but not dendritically targeting GABAergic synapses in the hippocampus (*25*). Perisomatically targeting CB_1R-positive basket cells (CB_1BCs) are implicated in proper neuronal ensemble formation underlying spatial coding and memory engrams (*28*–*30*). The abnormal development of CB_1BCs, or the in vivo exposure to Δ^9-tetrahydrocannabinol (THC), the psychoactive CB_1R ligand in cannabis, both disrupt the temporal synchronicity in the spiking of hippocampal neuronal assemblies (*28*, *31*). To support the temporal coordination of neuronal ensembles, it is conceivable that the synaptic cannabinoid tone plays an important role in the postsynaptic neuron–specific calibration of GABA release probability (Pr). Moreover, it also poses the question of whether THC affects synaptic activity by impairing the nanoscale functional organization of tonic cannabinoid signaling.

Despite its physiological and pathological significance, the mechanistic underpinnings and the precise functional organization of the synaptic cannabinoid tone remain elusive. Therefore, we developed a methodology to study single synapses between CB_1BCs and CA1 pyramidal cells (PCs) in mouse hippocampal slices by combining paired patch-clamp recordings with correlated confocal and stochastic optical reconstruction microscopy (STORM) super-resolution imaging. Our data show that neither of the principal endocannabinoid-synthesizing enzymes is required for tonic cannabinoid signaling. Instead, the nanoscale molecular stoichiometry of receptor/effector ratio at release sites determines how persistent CB_1R activity shapes synaptic variability. In vivo THC exposure impairs the nanoscale receptor/effector ratio and selectively eliminates the synaptic cannabinoid tone, but not phasic endocannabinoid signaling, emphasizing that nanodomain-specific molecular changes account for specific functional consequences of drug effects.

RESULTS

CB_1BC efferent synapses show target cell–specific variability

To determine whether the synaptic variability among CB_1BC output synapses is primarily driven by the presynaptic or the postsynaptic neuron, we first performed sequential paired recordings in the CA1 area (Fig. 1, A and B). One presynaptic interneuron and several postsynaptic PCs were filled with biocytin and Cascade Blue dye, respectively, for post hoc reconstruction of cellular and synaptic properties (Fig. 1C). Among the CB_1R-positive interneuron types, only CB_1BCs express tonic cannabinoid signaling (*25*). A presynaptic neuron was accepted as CB_1BC if its axon arbor was concentrated in the pyramidal layer [bouton distribution index (BDI) > 1; see Materials and Methods] and was immunolabeled for presynaptic CB_1Rs (Fig. 1, A and D). We visualized presynaptic active zones by immunofluorescence labeling for bassoon, a component of the release machinery (*5*, *32*). Together, 39 of 40 boutons forming close appositions with the somatodendritic surface of target cells contained bassoon accumulation at the side facing the postsynaptic neuron verifying the synaptic connections (Fig. 1D). Action potentials in a single presynaptic CB_1BC generated considerable variability in all parameters of the inhibitory postsynaptic currents (IPSCs) among the postsynaptic PCs (Fig. 1, B and E to G). Quantitative analysis uncovered that the large postsynaptic target cell–dependent variability in IPSC amplitudes and in successful synaptic events is not due to the variable number (2.6 ± 0.3) of synaptic connections (Fig. 1, H and I). Thus, the synaptic strength of the output synapses of individual CB_1BCs exhibits substantial differences between the postsynaptic target cells.

The presynaptic cannabinoid tone is a major factor in synaptic variability

We reasoned that the synaptic cannabinoid tone that requires postsynaptic neuroligin-3 and calcium signaling (*10*, *12*, *13*) would be an ideal mechanism to promote synaptic variability in a postsynaptic target cell–specific manner at CB_1BC efferent synapses. However, the necessity of CB_1Rs for this phenomenon has been challenged because CB_1R antagonists/inverse agonists, the traditional pharmacological tools that have been used to study tonic cannabinoid signaling, also potentiate $GABA_A$ receptors (*22*), activate G protein-coupled receptor 55 that regulate hippocampal GABAergic synapses (*21*, *24*), and are antagonists of mu-opioid receptors involved in retrograde synaptic plasticity (*23*, *33*). To directly assess whether CB_1Rs are necessary for the tonic control of GABA release, we performed paired recordings from CB_1BCs and CA1 pyramidal neurons in wild-type (WT) and littermate CB_1R-knockout (KO) mice. Bath application of the CB_1R antagonist/inverse agonist AM251 [(*N*-(piperidin-1-yl)-5-(4-iodophenyl)-1-(2,4-dichlorophenyl)-4-methyl1H-pyrazole-3-carboxamide)] (10 μM) readily increased the number of successful synaptic events and IPSC amplitudes in WT but not in KO mice (Fig. 2, A to D). Both the genetic inactivation and the pharmacological blockade of CB_1Rs strongly reduced the trial-to-trial variability [coefficient of variation (CV)] of IPSC amplitudes (Fig. 2E). AM251 application did not affect CV values in KO mice (Fig. 2E). Comparing the CV values, we estimated that the CB_1R-dependent synaptic cannabinoid tone is responsible for about one-third of synaptic variability ($33.6 \pm 10.7\%$) at perisomatic GABAergic synapses.

Because tonically active CB_1Rs were also reported to be present in the somatodendritic domain of hippocampal pyramidal neurons (*34*, *35*), we next aimed to determine the synaptic site of the cannabinoid tone expression. A change in Pr is reflected in altered $1/CV^2$ values and indicates a presynaptic locus of action (*36*). Accordingly, AM251 application caused larger $1/CV^2$ values calculated from the postsynaptic responses, revealing an increased Pr (fig. S1A). Moreover, multiphoton imaging demonstrated that AM251 significantly increased the amplitude of presynaptic Ca^{2+} transients in CB_1BC axon terminals in WT mice but had no effect in KO mice (fig. S1, B to D). Ca^{2+} transients were similar between genotypes after AM251 application indicating that molecular mechanisms determining calcium influx downstream of tonic CB_1R activity are not affected in KO mice ($n = 87$ and 46 boutons, $P_{ns} = 0.1$, Mann-Whitney *U* test). Together, these experiments provide direct evidence that presynaptic CB_1R activity tonically controls GABA release thereby substantially influencing target cell–dependent synaptic variability.

Cannabinoid tone remains intact the absence of the major endocannabinoid-synthesizing enzymes

Selective impairment of tonic, but not phasic forms of retrograde endocannabinoid signaling in the neuroligin-3 loss-of-function models of autism (*12*), indicates diverse mechanisms of presynaptic CB_1R engagement. Therefore, we next used KO mice of the respective endocannabinoid-synthesizing enzymes. In the absence of *N*-acyl phosphatidylethanolamine phospholipase D (NAPE-PLD), the principal AEA-synthesizing enzyme (*37*, *38*), neither the synaptic

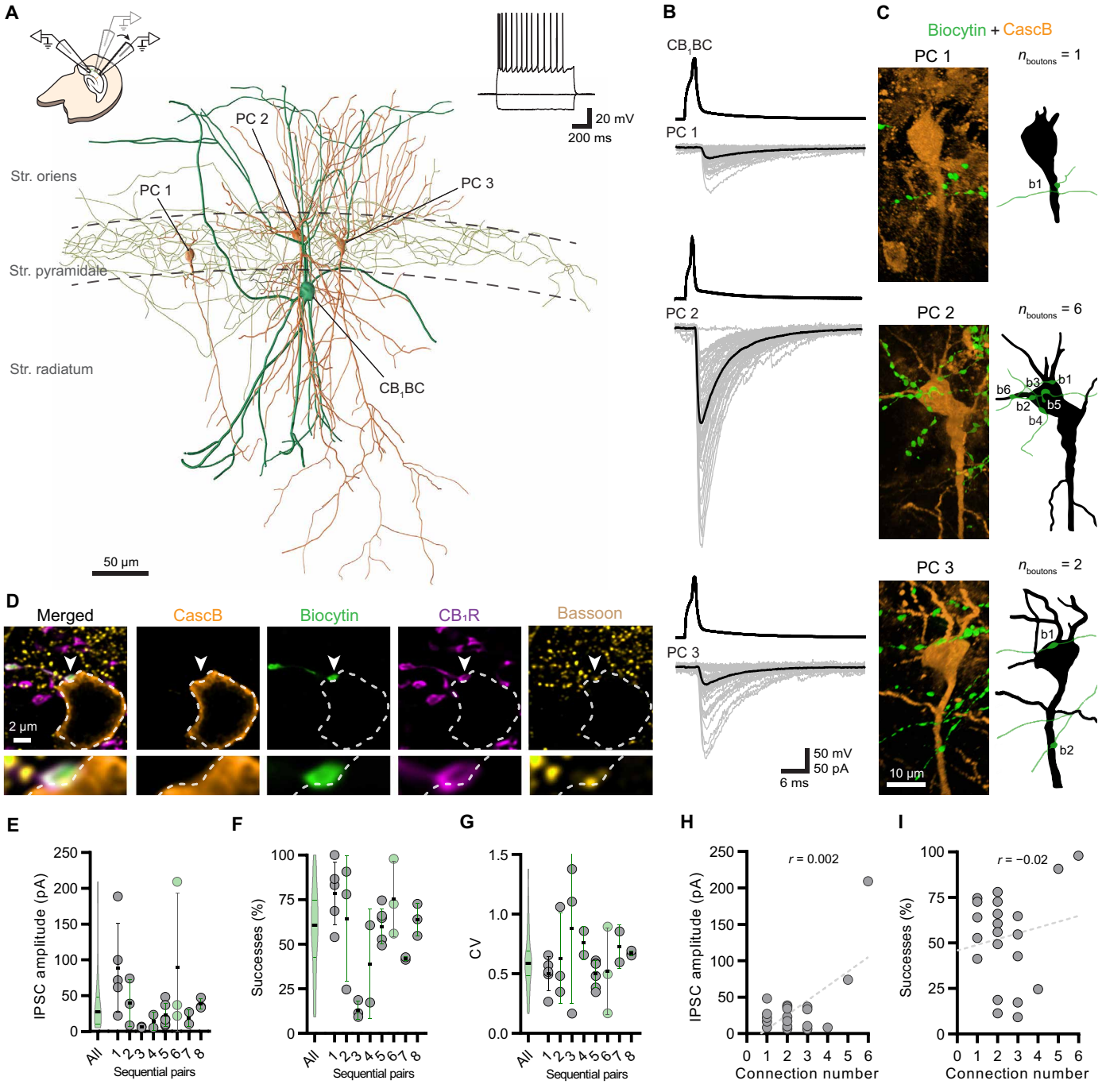

Fig. 1. Target cellspecific variability of CB_1BC efferent synapses. (**A**) Schematic illustration of experimental design. Inset traces show characteristic regular firing pattern of the CB_1BC in response to −200-, 0- and +300-pA current steps. Reconstruction of a CB_1BC (green) that is synaptically coupled to three postsynaptic PCs (orange). (**B**) Example traces of patch-clamp recordings from the three sequential pairs. Presynaptic APs evoked in the same CB_1BC (top traces) and the respective postsynaptic responses (bottom traces: 50 consecutive unitary IPSCs and their average effective unitary IPSC) that were recorded in subsequent PCs are shown. (**C**) Confocal three-dimensional (3D) maximum intensity projection images and reconstructions of CB_1BC axons (green) and PCs (orange) reveal the number and location of perisomatic connections (b1 to b6) between pairs. (**D**) Confocal images of quadruple staining demonstrate the presence of CB1R expression in the biocytin-labeled bouton (arrowhead) and show the accumulation of bassoon protein. Bottom insets show enlarged images of the synaptic connection. (**E** to **G**) Summary graphs show large variability in peak IPSC amplitude (E), number of successful events (F) and coefficient of variation (CV) of IPSCs (G) in sequential paired recordings ($n = 27$ pairs). Green data points depict the representative experiment presented on (A) to (D). Violin plots of pooled data show median ± interquartile range (IQR). Data presented as means ± SD. (**H** and **I**) The number of synaptic connections between pairs does not correlate with IPSC amplitude (H) or successes (I) ($n = 22$ pairs, IPSC amplitude: $P_{ns} = 0.99$, $r = 0.002$, successes: $P_{ns} = 0.91$, $r = -0.02$, Spearman's rank-order correlation).

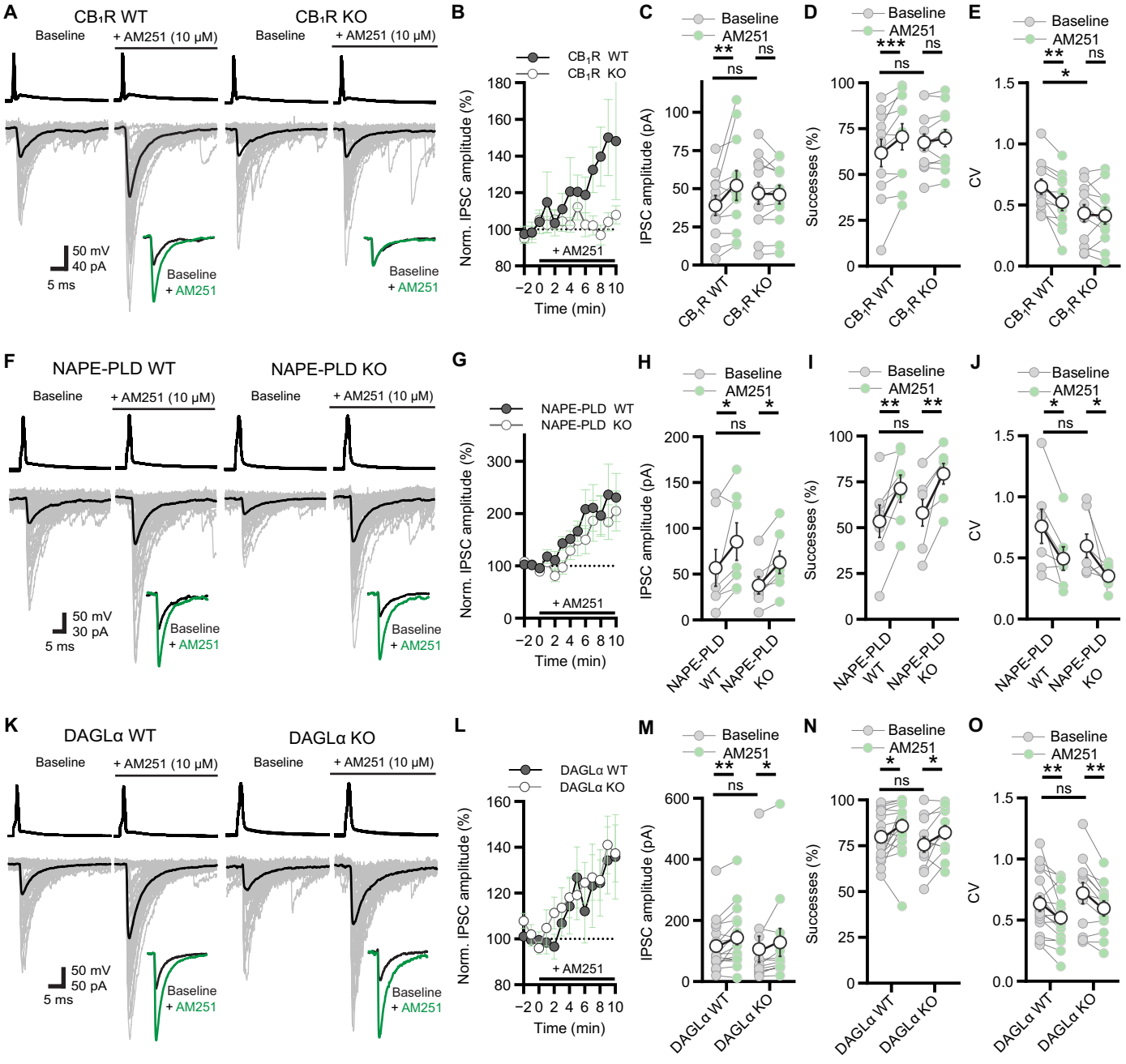

Fig. 2. Intact cannabinoid tone in absence of the major endocannabinoid-producing enzymes. (**A**) Representative traces of CB_1BC-PC paired recording obtained from CB_1R WT and KO mice during baseline and after AM251 application. Inset shows average IPSCs for easier comparison. (**B**) Summary plots of IPSC amplitudes during whole experiment. (**C**) Graph of IPSC amplitudes before and after AM251 application in CB_1R WT ($n = 11$ pairs, $^{**}P = 0.006$) and KO samples ($n = 12$ pairs, $P_{ns} = 0.86$). (**D**) Graph of successes in CB_1R WT ($^{***}P = 0.0003$) and KO ($P_{ns} = 0.25$). (**E**) Graph of relative variability of postsynaptic events measured by the CV of IPSCs in CB_1R WT ($^{**}P = 0.001$) and KO samples ($P_{ns} = 0.53$). Baseline CV differs between genotypes ($^{*}P = 0.03$). (**F**) Same as in (A), but in NAPE-PLD WT and KO samples. (**G**) AM251 increases IPSC amplitudes in both NAPE-PLD WT and KO. (**H**) Graph of IPSC amplitudes in NAPE-PLD WT ($n = 7$ pairs, $^{*}P = 0.02$) and KO ($n = 7$ pairs, $^{*}P = 0.04$). (**I**) Graph of successes in NAPE-PLD WT ($^{**}P = 0.009$) and KO ($^{**}P = 0.003$). (**J**) Graph of CV values in NAPE-PLD WT ($^{*}P = 0.02$), and KO ($^{*}P = 0.03$). (**K**) Same as in (A) but in DAGLα WT and KO samples. (**L**) AM251 increases IPSC amplitudes both in DAGLα WT and KO. (**M**) Graph of IPSC amplitudes in DAGLα WT ($n = 17$ pairs, $^{**}P = 0.003$) and KO ($n = 12$ pairs, $^{*}P = 0.03$). (**N**) Graph of successes in DAGLα WT ($^{*}P = 0.003$) and KO ($^{*}P = 0.004$). (**O**) Graph of CV values in DAGLα WT ($^{**}P = 0.02$) and KO ($^{**}P = 0.05$). Two-way analysis of variance (ANOVA) with repeated measures is shown; graphs show means ± SEM with individual values.

cannabinoid tone (Fig. 2, F to J) nor depolarization-induced suppression of inhibition (DSI), a phasic form of endocannabinoid-mediated synaptic plasticity, was affected (fig. S2, A and D). In the absence of DAGLα, the principal 2-AG–synthesizing enzyme (*39*), DSI was absent as shown before (*15*) (fig. S2, A and D), but there was no change in the synaptic cannabinoid tone (Fig. 2, K to O). Liquid chromatography–tandem mass spectrometry in hippocampal slice preparations used for electrophysiological experiments excluded homeostatic compensation in endocannabinoid levels (fig. S2, B and C). In addition, patch-clamp recordings revealed intact cannabinoid tone in NAPE-PLD/DAGLα double-KO mice (fig. S3).

Endocannabinoids are important tonic regulators of neurotransmitter release in a circuit-wide manner under specific physiological or pathological conditions (*16*–*19*, *40*). Accordingly, bath application of JZL184, an inhibitor of the 2-AG–degrading enzyme monoacylglycerol lipase (MAGL), robustly increased 2-AG levels by ~250% and concomitantly decreased IPSC amplitudes and successful synaptic events in WT mice. In contrast, JZL184 effects were completely absent in DAGLα KO mice (fig. S4, A to D). These findings demonstrate that there are mechanistically different forms of tonic cannabinoid signaling even at the same synapse type. While the 2-AG tone requires DAGLα activity, similarly to the well-established phasic forms of endocannabinoid signaling (*15*), the specific form of cannabinoid tone contributing to postsynaptic target cell–specific synaptic variability is independent of the activity of the two major endocannabinoid-producing enzymes. Hereafter, we use the terms "endocannabinoid" and "cannabinoid" to distinguish between the AEA/2-AG tones and the NAPE-PLD/DAGLα–independent synaptic cannabinoid tone, respectively.

Nanoscale receptor/effector stoichiometry determines the synaptic cannabinoid tone

To identify an alternative mechanism that distinguishes the synapse-specific cannabinoid tone from other forms of phasic and tonic endocannabinoid signaling, we considered that heterotrimeric guanine nucleotide–binding protein–coupled receptors (GPCRs) spontaneously exist in a suite of inactive and active conformations. Because there is a preexisting equilibrium between constitutively active and inactive GPCR conformations (*41*), we reasoned that if constitutive CB_1R activity contributes to the synaptic cannabinoid tone, then the molecular abundance of CB_1Rs on the axon terminal should predict the magnitude of the cannabinoid tone.

As an indirect support for this reasoning, bath application of a single concentration of a neutral CB_1R antagonist did not affect perisomatic GABAergic synapses (*25*). However, the absence of effect of a pharmacological tool has limitations for interpretation. As an argument against this reasoning, there was no correlation between CB_1R levels and its potency on downstream signaling when CB_1R density on axon terminals was measured by confocal microscopy (*26*). Therefore, to more directly test the hypothesis that presynaptic CB_1R density alone is sufficient to predict the cannabinoid tone and Pr, we developed a workflow for the correlative measurement of physiological parameters, morphological data, and molecular distributions at the nanoscale level within a unitary GABAergic synapse (Fig. 3A). We carried out paired recordings from CB_1BCs and CA1 pyramidal neurons and recorded IPSCs before and after AM251 application to measure the magnitude of the synaptic cannabinoid tone (Fig. 3B). The presynaptic basket cell and the postsynaptic pyramidal neuron were filled with biocytin and Cascade Blue, respectively. The neuronal processes were anatomically reconstructed at high magnification to determine all synaptic connections (Fig. 3, C and D). Pairs that were connected only with a single synapse that contained one confocal bassoon cluster (identified via neighboring bassoon-positive voxels in the confocal image) located opposite to the postsynaptic neuron were selected for STORM imaging. The z-stack image of the synaptic connection was acquired by volumetric three-dimensional (3D)–STORM super-resolution imaging to visualize the synapse regardless of bouton orientation (Fig. 3, E and F). CB_1R nanoscale density was calculated in relation to the active zone visualized by bassoon immunolabeling, because bassoon has stoichiometric relationship with other release machinery components including voltage-gated calcium channels (*5*, *42*) (Fig. 4A). To determine the number of functional release sites within a single active zone, we performed variance-mean analysis in a separate set of experiments (fig. S5 and Materials and Methods). Quantal analysis revealed low baseline Pr and an average of three functional release sites per bouton (3.07 ± 0.57; $n = 10$ pairs) (fig. S5I) matching the number of individual release machineries (3.2) in the same axon terminal population identified by super-resolution imaging of bassoon (*43*). Therefore, the Pr value was estimated from the success ratio of IPSCs assuming three functional release sites per active zone. Collectively, this correlative workflow enables direct quantification of the nanoscale abundance of CB_1Rs that accounts for the impact of the synaptic cannabinoid tone on neurotransmitter release within a single synapse.

Correlated measurements of the estimated Pr, the active zone size, and the number of CB_1Rs along the entire bouton surface revealed that the total CB_1R number on the axon terminal alone does not predict Pr (Fig. 4B). Bassoon voxel numbers also did not correlate with Pr (Fig. 4C). These observations suggest that instead of a single molecular parameter, the stoichiometric relationship of the regulatory receptor and its effectors may better predict how constitutive CB_1R activity controls neurotransmitter release. This also implies that the nanoscale physical distance between the receptor and its effectors strongly affects potency. As an indirect indication, we found cell type–specific differences in CB_1R density adjacent to the release sites on GABAergic boutons when electrophysiologically characterized single neurons were studied (*43*). Therefore, we next aimed to experimentally test the hypothesis that the nanoscale stoichiometric ratio may be the key determinant of the magnitude of the synaptic cannabinoid tone and its influence on GABA release by performing paired patch-clamp recording and subsequent super-resolution imaging from the very same unitary synapse.

When the nanoscale stoichiometry parameter was calculated by measuring the ratio of intra/perisynaptic CB_1Rs and bassoon-positive voxels, we found a strong inverse correlation with the estimated release probability suggesting that the more CB_1Rs are active in the nanoscale vicinity of the release machinery, the smaller the Pr is. Moreover, there was a steep decrease in the correlation coefficient value more than 200 nm away from the active zone, highlighting the specific importance of the nanoscale physical distance (Fig. 4, D and E). The correlative relationship depends on the persistent functional activity of intra/perisynaptic CB_1Rs, because subsequent AM251 administration eliminated the correlation between the receptor/effector ratio and the Pr in the same recorded pairs without altering the CB_1R/bassoon nanoscale relationship (Fig. 4F and fig. S6). In addition, the nanoscale stoichiometry positively scaled with the effect of AM251. In other words, the more intra/perisynaptic CB_1Rs

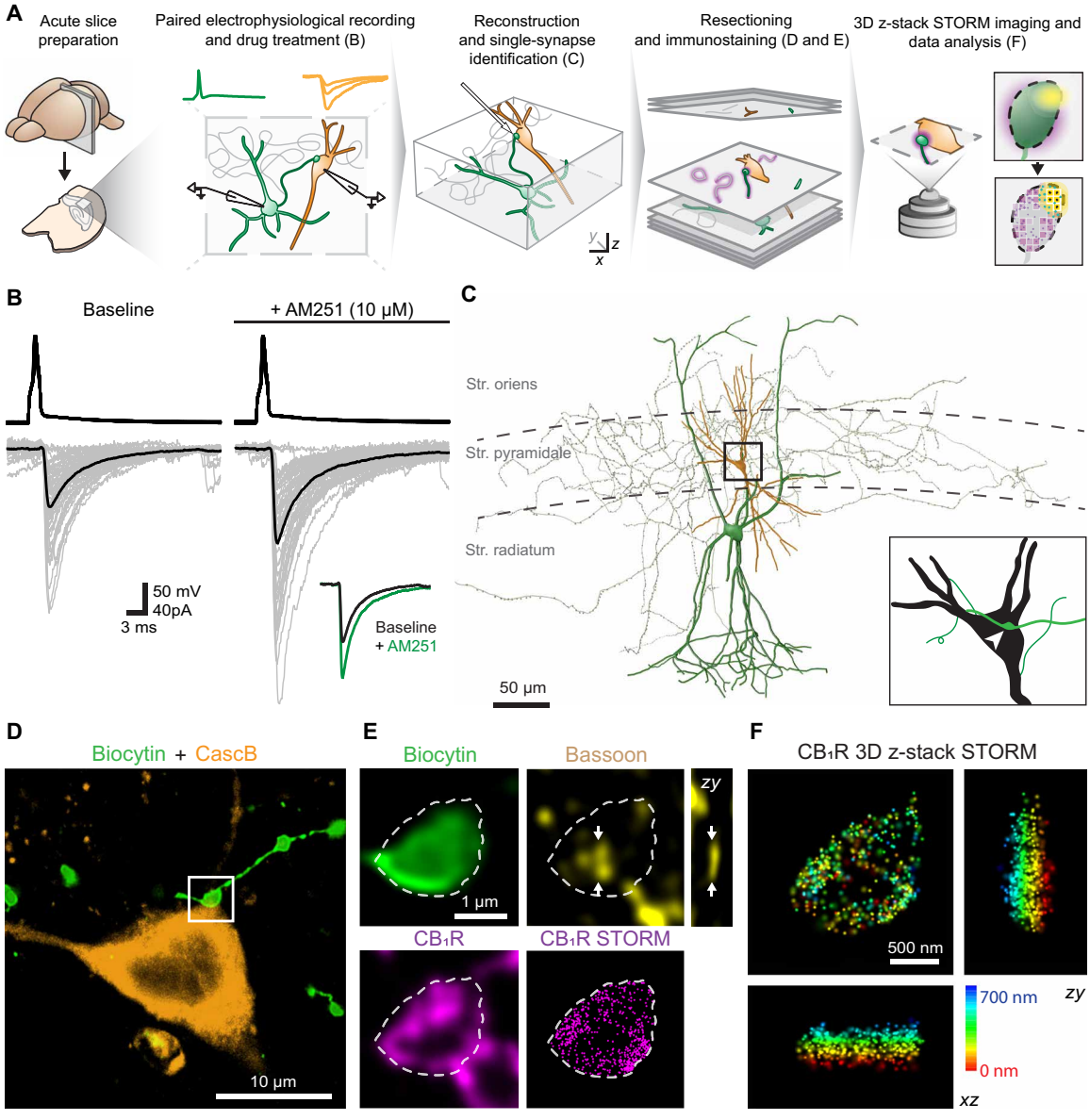

Fig. 3. Correlated electrophysiological, anatomical, and nanoscale molecular analysis of unitary CB_1BC-PC synapses. (**A**) Schematic workflow of the experimental procedure. (**B**) Example traces of paired recording reveals baseline properties of synaptic transmission and tonic cannabinoid signaling. (**C**) Morphological reconstruction of the recorded CB_1BC (biocytin, green) and PC (CascB, orange). (**D**) Confocal microscopical image of single identified synaptic connection between recorded cells (arrowhead). (**E**) Boxed region in (D) is shown at higher magnification after immunostaining. Correlated confocal and STORM super-resolution imaging of the biocytin-filled axon terminal (green) was used to identify the presynaptic active zone (arrows) by bassoon-immunolabeling (yellow) and was exploited to quantify the nanoscale distribution of CB_1Rs (magenta). Arrows on zy view of bassoon channel indicate slice plane as well. (**F**) 3D z-stack STORM of the identified CB_1R-positive axon terminal.

control the release machinery, the larger the impact of synaptic cannabinoid tone on the release probability. Accordingly, low-Pr unitary synaptic connections were associated with a stronger cannabinoid tone (Fig. 4, G and H). These measurements together provide insights into the qualitative and quantitative nature of how constitutively active metabotropic receptors control neurotransmitter release.

Reduced CB_1Rs mobility is observed in nanodomains

Synapse-specific differences in nanoscale stoichiometry imply that axon terminals regulate the functional availability of the intra/perisynaptic CB_1R population. CB_1Rs are present throughout the entire axon arbor surface and exhibit dynamic molecular diffusion with a different microdomain-level mobility in the axonal compartment and in axon terminals (*43*, *44*). Therefore, we reasoned that the constitutively active CB_1R population may have reduced mobility at the nanodomain level for efficient coupling to the release machinery. To test this implication, we measured CB_1R mobility by using nanoPaint single-particle quantum dot (QD) tracking (*45*) that allows 3D reconstruction of the boutonal surface with nanoscopic resolution and calculated the translocation distances between

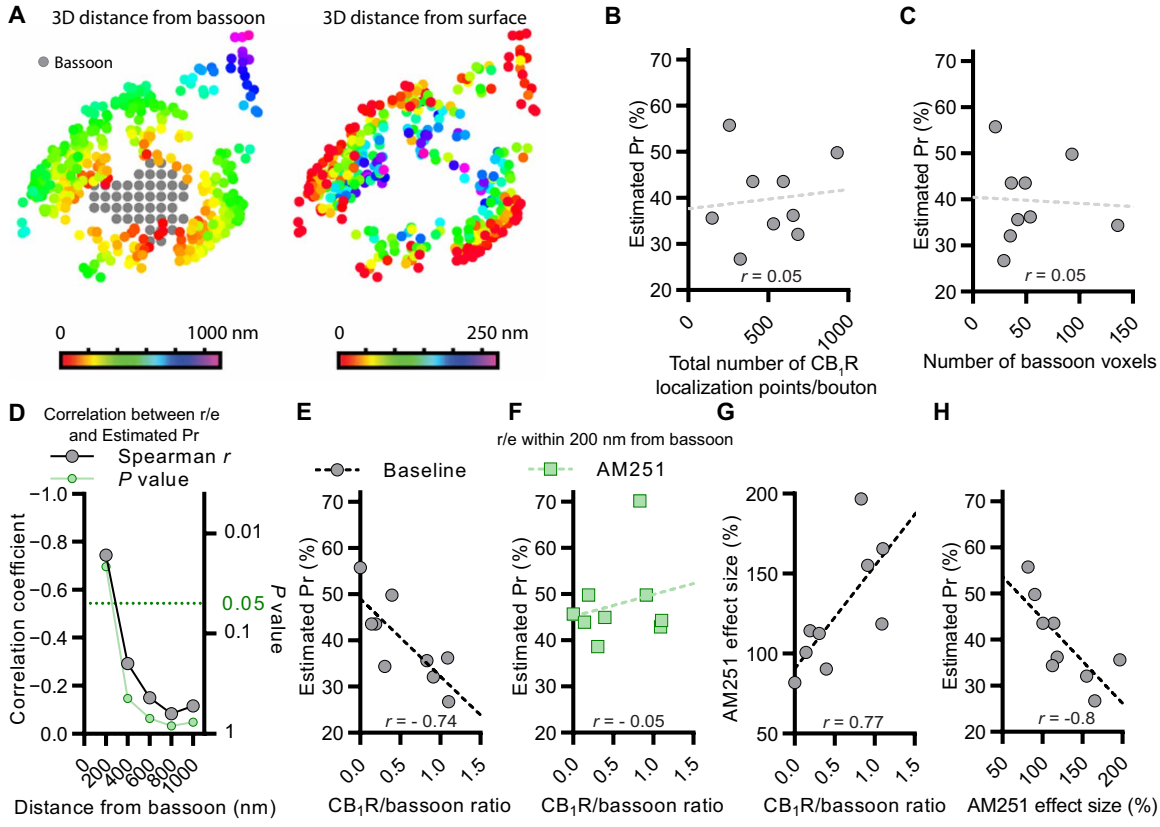

Fig. 4. Nanoscale receptor/effector stoichiometry determines the synaptic cannabinoid tone. (**A**) 3D z-stack STORM data were used to calculate the nanoscale distance of each CB_1R from the bassoon-positive voxels and from the surface of the axon terminal. (**B**) The total number of CB_1Rs on the axon terminal does not predict the estimated Pr ($n = 9$ pairs, $P_{ns} = 0.90$, $r = 0.05$). (**C**) The number of bassoon voxels does not covary with the estimated Pr ($P_{ns} = 0.90$, $r = 0.05$). (**D**) Correlation coefficients of the CB_1R/bassoon stoichiometry calculated at various distances from bassoon labeling. The receptor/effector stoichiometry scales with the estimated Pr in a nanoscale distance-dependent manner. (**E**) Correlation plot shows an inverse correlation between the estimated Pr and the nanoscale CB_1R/bassoon ratio measured within 200-nm distance from the active zone (*$P = 0.03$, $r = -0.74$). (**F**) Application of AM251 impairs the inverse correlation between the estimated Pr and the nanoscale CB_1R/bassoon ratio at the same recorded pairs as shown at baseline on (E) ($P_{ns} = 0.90$, $r = -0.05$). (**G**) Correlation plot shows positive correlation with the nanoscale CB_1R/bassoon ratio and the strength of the synaptic cannabinoid tone (*$P = 0.02$, $r = 0.77$). (**H**) Plot shows negative correlation between the strength of the synaptic cannabinoid tone and the estimated Pr (*$P = 0.01$, $r = -0.8$, Spearman rank-order correlation).

consecutive frames for receptor diffusion estimation (Fig. 5A and Materials and Methods). The average translocation distances were significantly shorter in boutons compared to axons, as previously demonstrated (*44*) (Fig. 5B). Moreover, we also found that short (<100 nm) and long (>100 nm) translocations of CB_1Rs representing reduced or enhanced mobility, respectively, were topologically segregated within the axon terminals but not along the axons (Fig. 5C). In addition, only short translocations exhibited anisotropic distribution, whereas no such enrichment was detected for long translocations (Fig. 5C). Furthermore, Ripley's *K*-function analysis revealed the clustering of short translocations only in boutons but not in axons (Fig. 5D). In contrast, there was no indication of any clustering of CB_1Rs with long translocations in either subcellular compartment (Fig. 5D). The apparent clustering of CB_1Rs with a slower diffusion rate manifests below the diffraction level at 100 nm and already disappears at 300 nm (Fig. 5E). Together, these live-cell imaging observations demonstrate that CB_1R diffusion is substantially slowed within a nanodomain on the surface of axon terminals and that reduced diffusion enriches CB_1R clusters that may support coupling to downstream effector proteins.

Selective reduction of extrasynaptic CB_1R abundance does not affect the cannabinoid tone

If nanodomain-specific CB_1R activity is responsible for the synaptic cannabinoid tone, then selective perturbation of intra- versus extrasynaptic CB_1R abundance would differentially affect this synaptic phenomenon. By using Western blot in electrophysiological slice preparations, we found that CB_1R heterozygous (HET) mice have ~50% less CB_1R protein compared to littermate WT mice (Fig. 6A). Because CB_1Rs are present in many cell types and protein levels may change in a cell type–specific manner, we measured CB_1R immunolabeling on perisomatically targeting GABAergic axon terminals by STORM imaging (Fig. 6B). While bouton size and active zone size were not affected by genotype (Fig. 6, C and D), the number of localization points (LPs) representing CB_1R proteins along the entire bouton surface was strongly reduced in HET mice (Fig. 6E). In contrast, CB_1R numbers in the nanoscale vicinity of bassoon clusters were similar in both genotypes, suggesting that axon terminals first fill up the intra/perisynaptic CB_1R population (Fig. 6F). Moreover, the nanoscale receptor/effector ratio was also comparable between WT and HET mice (Fig. 6G). Notably, paired recordings showed

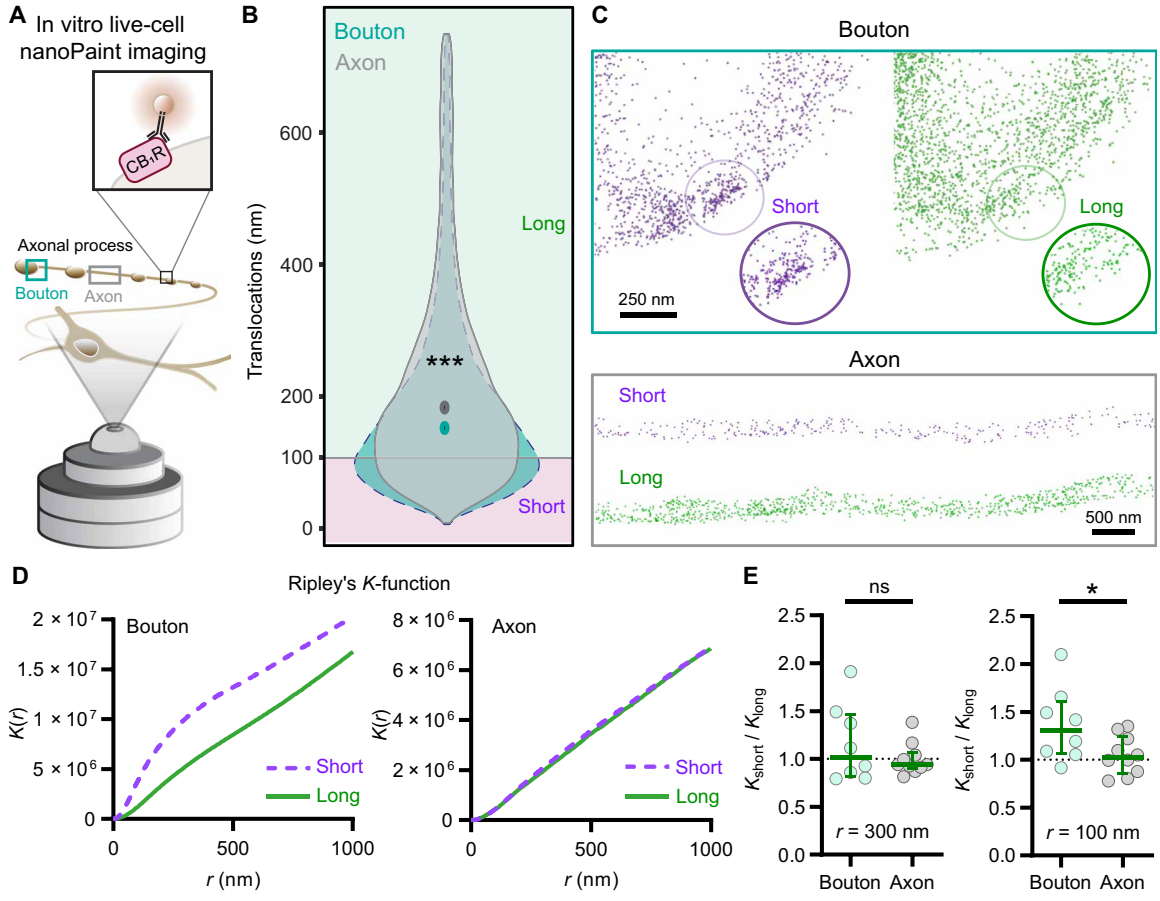

Fig. 5. Nanoscale concentration of CB_1Rs with reduced mobility. (**A**) Schematic representation of experimental design. (**B**) Violin plots and medians of translocations obtained from boutons and axonal segments ($n = 8$ boutons and 10 axons, $^{***}P < 0.001$, Mann-Whitney U test). (**C**) Visualization of single-particle tracking of labeled CB_1Rs was conducted in the boutonal profiles (cyan box) and interboutonal segments (gray box) of the axonal process. CB_1Rs were categorized by their movement as either short translocation distances (0 to 100 nm) in magenta or as long translocations (100 to 750 nm) in green. (**D**) Multidistance spatial cluster analysis by using Ripley's $K(r)$ plot of short and long CB_1R translocations revealed clustered nanoscale distribution pattern of short trajectory CB_1Rs but not the long trajectory CB_1Rs in the boutons [cyan box on (A) and (C)]. Neither the short translocations nor the long translocations of individual CB_1Rs differed from the expected K value in axons [gray box on (A) and (C)]. (**E**) Summary graphs show the quotient of Ripley's K-function within a radius of 300 and 100 nm in boutons and in axons ($n = 8$ boutons and 10 axons, $P_{ns} = 0.27$, unpaired t test). The quotient of Kshort/Klong for a radius of 100 nm is higher in boutons than in axons ($n = 8$ boutons and 10 axons, $^{*}P = 0.04$, unpaired t test). Graphs show means ± SEM with individual values.

that the cannabinoid tone and its impact on synaptic variability were not affected in HET mice despite the substantially lower extrasynaptic CB_1R density (Fig. 6, H to K, and fig. S7).

THC disrupts the intrasynaptic nanoscale stoichiometry and the cannabinoid tone

The complex behavioral effects of cannabis are largely due to the activation of CB_1Rs by THC, the psychoactive phytocannabinoid substance. By cell type–specific STORM imaging, we previously found that in vivo THC administration causes strong dose-dependent reduction in the total CB_1R content of CB_1BC boutons (*43*). However, our findings in HET mice revealed that a robust reduction of CB_1Rs in axon terminals measured at the microdomain level may not necessarily have functional consequences on synaptic transmission. Conversely, if THC exposure compromises the intrasynaptic nanoscale stoichiometry, then changes in the cannabinoid tone would be expected. To address this question, we repeated the THC administration paradigm that was optimized to study behavioral tolerance in mice (Materials and Methods). After in vivo THC treatment, ex vivo biocytin-filled CB_1BCs were processed for correlated confocal and STORM imaging (Fig. 7, A and B). There was no change in the size of axon terminals and active zones (Fig. 7, C and D). In contrast, THC administration caused a significant decrease in overall CB_1R numbers (Fig. 7E). The magnitude of reduction in total CB_1R abundance was comparable in HET mice and after THC treatment (38% versus 47%). In notable contrast to the observations in HET mice, we found a marked decrease in the intra/perisynaptic CB_1R population and in the nanoscale receptor/effector ratio after THC exposure in both the CA1 and CA3 areas (Fig. 7, F and G, and fig. S8). Paired patch-clamp recordings in hippocampal slices obtained from THC-treated mice revealed robust changes in the basic synaptic physiological properties (Fig. 7H). The synaptic cannabinoid tone was completely absent. AM251 application could not increase IPSC amplitudes and the number of successful events in line with the strong increase in baseline parameters (Fig. 7, I to K). The decrease in CV values and their insensitivity to AM251

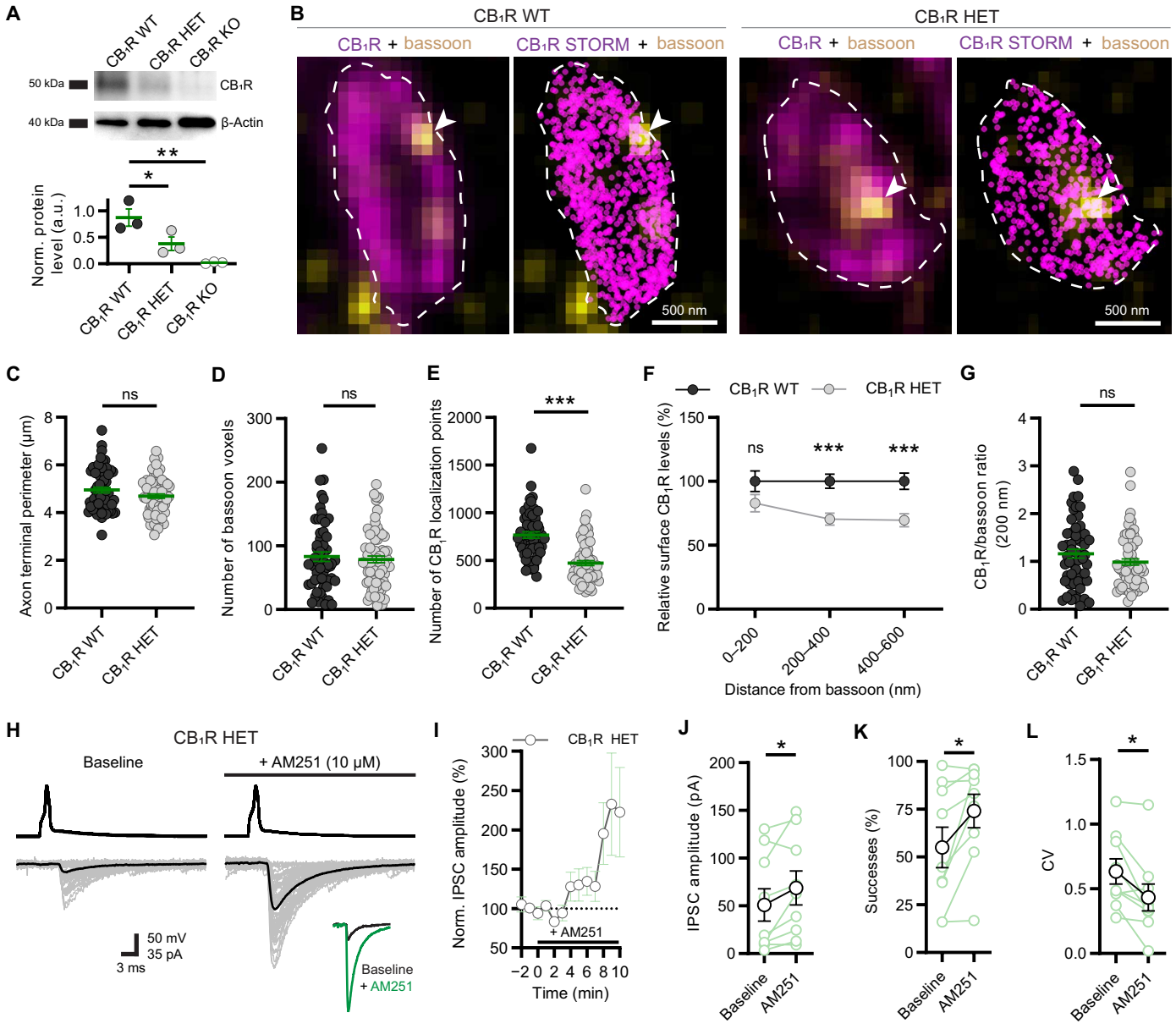

Fig. 6. Selective reduction of extrasynaptic CB_1R abundance does not affect the cannabinoid tone. (**A**) Western blot of WT, CB_1R heterozygotes (HET), and CB_1R KO hippocampal lysates ($n = 3$ animals per genotype, $^*P = 0.046$ between WT and HET, $^{**}P = 0.04$ between WT and KO, one-way ANOVA with Dunnett's multiple comparisons test). (**B**) Confocal images show immunolabeling for CB_1R (magenta) and the active zone (arrowhead) labeled via bassoon protein (yellow), whereas the corresponding STORM super-resolution images display the nanoscale distribution of CB_1Rs in axon terminals. (**C**) Summary graph of the perimeter of axon terminals in WT and HET samples (WT: $n = 57$ boutons, HET: $n = 71$ boutons, $P_{ns} = 0.18$). (**D**) Summary graph of the number of bassoon-positive voxels shows identical active zone size in the axon terminals of WT and HET mice ($P_{ns} = 0.94$). (**E**) Summary graph of the total number of CB_1R localization points (NLP) on axon terminals measured with STORM ($^{***}P < 0.0001$). (**F**) Summary graph of distance-dependent decrease of CB_1Rs on the surface of boutons in HET mice (0 to 200 nm: $P_{ns} = 0.08$, 200 to 400, 400 to 600 nm: $^{***}P < 0.0001$). (**G**) Summary graph of nanoscale CB_1R/bassoon ratio in the vicinity (200 nm) of the active zone ($P_{ns} = 0.17$). (**H**) Representative traces from paired recordings obtained from HET mice before and after the application of AM251. (**I**) Summary plots of whole experiments show increase of IPSC amplitudes in HET samples after AM251 application. (**J**) Summary graph of IPSC amplitudes before and after application of AM251 in HET ($n = 9$ pairs, $^*P = 0.04$). (**K**) Summary graph of successful postsynaptic events in HET ($^*P = 0.02$). (**L**) Summary graph of CV values in HET ($^*P = 0.02$). Graphs show means ± SEM with individual values. [(C) to (G)] Mann-Whitney *U* test; [(J) to (L)] Wilcoxon signed-rank test.

revealed that THC also diminishes synaptic variability (Fig. 7L). In contrast, phasic endocannabinoid signaling (DSI) was only mildly affected and remained sensitive to AM251 (Fig. 7, M and N).

These results demonstrate that THC exposure impairs the precise nanoscale functional organization that underlies the synaptic cannabinoid tone and reduces the synapse-specific variability of CB_1BC output synapses. These findings also highlight the importance of nanodomain-specific measurements for providing physiologically and pathologically relevant insights into drug-induced molecular changes.

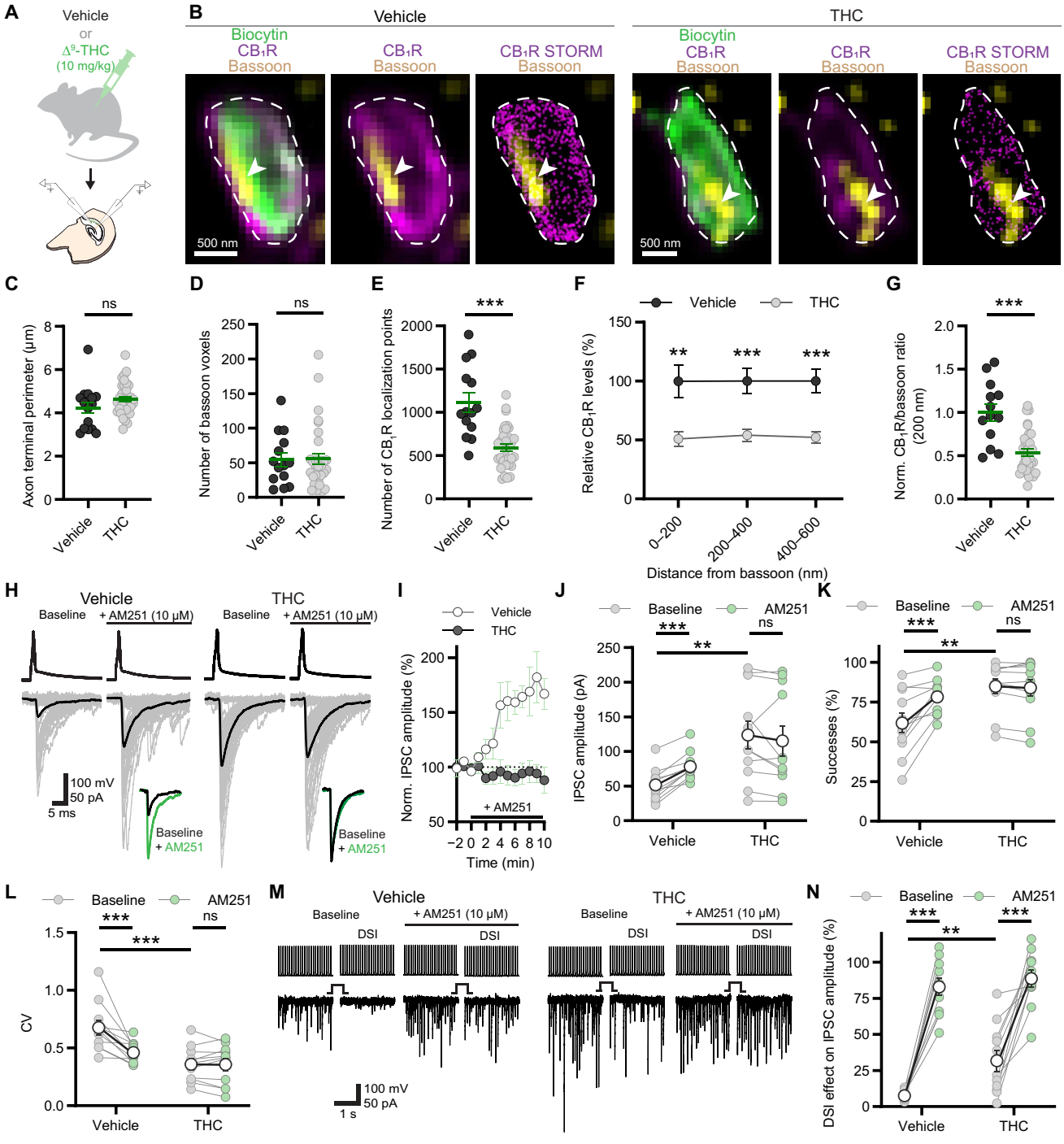

Fig. 7. THC disrupts the intrasynaptic nanoscale stoichiometry and the cannabinoid tone. (**A**) Schematic illustration of experimental design. (**B**) Confocal and combined STORM images of CB_1R labeling (magenta) on biocytin-labeled (green) boutons from either vehicle or THC-treated animals. Arrowhead marks bassoon-labeled synaptic active zone (yellow). (**C**) Summary graph of axon terminal perimeter in vehicle and THC-treated samples (vehicle: $n = 16$ boutons, THC: $n = 35$ boutons, $P_{ns} = 0.14$). (**D**) Summary graph of bassoon-positive voxel numbers (vehicle: $n = 14$ boutons, THC: $n = 32$ boutons, $P_{ns} = 0.84$). (**E**) Summary graph of CB_1R STORM localization point numbers (NLP) (***$P < 0.0001$). (**F**) Summary graph of distance-independent decrease of CB_1Rs on the bouton surface in THC-treated mice. (0 to 200 nm: **$P = 0.002$, 200 to 400, 400 to 600 nm: ***$P < 0.0001$) (**G**) Summary graph of CB_1R/bassoon ratio in vehicle and THC-treated boutons (***$P = 0.0001$). (**H**) Example traces of paired recordings before and after AM251 application from slices of in vivo vehicle or THC-treated mice. (**I**) Summary plots of IPSC amplitudes during whole experiment. (**J**) Summary graph of IPSC amplitudes during baseline and after application of AM251 in vehicle- or THC-treated groups ($n = 11$ pairs per group, ***$P = 0.0004$, $P_{ns} = 0.18$, baseline difference: **$P = 0.002$). (**K**) Summary graph of successes (***$P < 0.0001$, $P_{ns} = 0.74$, baseline difference: **$P = 0.002$). (**L**) Summary graph of IPSC CV values (***$P < 0.0001$, $P_{ns} = 0.96$, baseline difference: ***$P < 0.0001$). (**M**) Representative IPSC responses on DSI before and after AM251 application on vehicle- or THC-treated slices. (**N**) Summary graph of DSI effect on IPSC amplitudes (***$P < 0.0001$, baseline difference: **$P = 0.004$). Graphs show means ± SEM with individual values. [(C) to (G)] Mann-Whitney *U* test; [(J) to (N)] two-way ANOVA with repeated measures.

DISCUSSION

To better understand how postsynaptic neurons control neurotransmitter release via retrograde signaling, we designed a methodology that elucidates the nanoscale molecular organization underlying specific synaptic processes. We first defined the presynaptic nanoscale components of a specific form of retrograde cannabinoid signaling and subsequently determined how the psychoactive substance in cannabis dismantles the nanoscale architecture that calibrates neurotransmitter release in a synapse-specific manner.

The qualitative and quantitative properties of neurotransmitter release are established by numerous physical, chemical, and biological parameters that together determine intricate synapse-specific differences (*46*–*48*). Our results showed that the synaptic cannabinoid tone also contributes to synaptic variability. Because synapses with larger presynaptic variance have enhanced learning rates (*49*), this CB_1R-dependent synaptic phenomenon can influence the dynamic tunability of synapses for cognitive processes. This is important because the synaptic cannabinoid tone is exemplified in CB_1BCs output synapses that are implicated in neuronal ensemble formation and are affected in several psychiatric disorders (*12*, *13*, *28*–*30*, *50*). For example, the synaptic cannabinoid tone may serve to filter firing frequency-related distinct bandwidth of signals and thus selectively modulate behavioral state-dependent neuronal communication depending on the initial presynaptic Pr in a connection-specific manner in neuronal ensembles (*11*, *51*–*53*).

The importance of the cannabinoid tone in adjusting target cell–dependent synaptic strength indicates the existence of a synapse-specific retrograde mechanism. We identified the intrasynaptic nanoscale stoichiometry parameter that is sufficient to predict the magnitude of the synaptic cannabinoid tone and its influence on GABA release. The observation that the CB_1R inverse agonist/antagonist AM251 disrupts the correlation between the estimated Pr and the nanoscale receptor/effector ratio suggests that the high correlation coefficient requires persistent CB_1R activity. This is further supported by the strong positive correlation between the effect of AM251 and the nanoscale receptor/effector ratio. The molecular stoichiometry of the presynaptic release machinery is precisely organized, and bassoon-containing nanomodules correlate with experience-dependent structural plasticity (*5*, *54*, *55*). As a limitation, we used polyclonal primary and secondary antibodies that introduce technical variability. Therefore, it is expected that further technological improvements, such as the application of stoichiometrically binding fluorescently tagged small-molecule probes for super-resolution imaging (*56*), will reveal an even more precise nanoscale order in the molecular arrangement of retrograde cannabinoid signaling. An independent line of evidence based on genetic (CB_1R HET mice) and pharmacological (THC) perturbation approaches also pointed to the pivotal role of the size and functional availability of the intrasynaptic CB_1R population. It is important to emphasize that the intra- and extrasynaptic CB_1R populations most likely do not represent static receptor pools. Instead, CB_1Rs are dynamically diffusing on the surface of axons and axon terminals (*44*). As our live-cell imaging experiments demonstrated, the mobility of CB_1Rs is substantially reduced within a diffraction-limited nanodomain. It is conceivable that CB_1Rs immobilized in the nanoscale vicinity of the release site have more robust functional impact on basal synaptic transmission because the synaptic cannabinoid tone relies on membrane-delimited beta/gamma subunit signaling and inhibition of presynaptic N-type calcium channels (*27*, *57*). This suggests that synapses may be capable of regulating the size of their intrasynaptic CB_1R population by specific mechanisms. For example, the cannabinoid tone, but not phasic forms of retrograde endocannabinoid signaling, requires intact postsynaptic neuroligin-3 function (*12*, *13*). Thus, trans-synaptic protein-protein interactions that are well known to regulate constitutive GPCR activity (*58*) may be ideal synapse-specific candidate mechanisms to determine how many tonically active intrasynaptic CB_1Rs control the release machinery. One candidate is neuroligin-3 that is essential for tonic cannabinoid signaling at these synapses (*12*) and plays a key role in controlling the nanoscale organization of central synapses (*59*). Notably, neuroligin-3 is selectively expressed at CB_1R-expressing inhibitory synapses in the CA1 region of the hippocampus (*60*). Future studies may also test the possibility whether certain intracellular CB_1R-interacting proteins, such as the Src homology 3-domain growth factor receptor-bound 2-like (endophilin) interacting protein 1 (SGIP1), Wiskott-Aldrich syndrome protein-family verprolin-homologous protein 1 (WAVE1) complex, intracellular protein BiP and growth-associated protein of 43 kDa (GAP43) may also regulate the cannabinoid tone specifically in the intrasynaptic active zone at perisomatic synapses (*61*–*65*). The cannabinoid receptor-interacting protein 1a (CRIP1a) is an especially interesting candidate, because it is present at inhibitory synapses in the hippocampus and was shown to affect tonic CB_1R activity in cellular preparations (*66*–*68*). The synapse-specific distribution of the multiple CB_1R-interacting proteins may also play an instrumental role in how CB_1Rs are segregated into intra/peri- and extrasynaptic populations and become associated with distinct downstream signaling mechanism that organize the cytoskeleton (*69*) or regulate the number of vesicles (*70*). Alternatively, part of the dense extrasynaptic population may also represent a reservoir pool that contributes to the rapid recycling of active receptors that is generally known to be important for presynaptic metabotropic receptors (*71*).

Our findings also revealed that NAPE-PLD and DAGLα, the two main endocannabinoid-producing enzymes, are not required for the synaptic cannabinoid tone. Certainly, the existence of an unknown lipid, peptide, or gaseous retrograde messenger can never be fully excluded, but we argue that the two traditional endocannabinoid messengers are unlikely to be involved in this phenomenon. While AEA can be synthesized through complex enzymatic pathways in biochemical preparations (*72*), NAPE-PLD is known to be the primary enzyme responsible for the synthesis of AEA in vivo (*37*, *38*). Accordingly, recent evidence showed that NAPE-PLD is responsible for the AEA tone in the stress response (*19*, *38*). However, we found that the synaptic cannabinoid tone is unaffected in NAPE-PLD KO mice. Alpha/beta hydrolase domain-containing protein 4 (ABHD4), a serine hydrolase mediating the first step in the alternative AEA synthesis route, is expressed in the embryonic brain (*73*), rendering this pathway also unlikely to be responsible for the synaptic cannabinoid tone. Furthermore, inhibition of fatty acid amide hydrolase, the AEA-degrading enzyme, does not affect the same GABAergic synapses per se but inhibits the 2-AG tone via postsynaptic transient receptor potential vanilloid 1 activation (*25*). In the case of 2-AG, three potential synthesizing enzymes have been detected in biochemical preparations. ABHD6 is an unlikely candidate because it was originally described as a 2-AG–degrading enzyme at excitatory synapses as an auxiliary component of AMPA receptors and requires high substrate concentrations to reverse its activity for 2-AG synthesis (*74*–*76*). DAGLβ is an intracellular

serine hydrolase that is primarily present in microglia (*77*), whereas tonic cannabinoid signaling requires intact postsynaptic calcium signaling and neuroligin-3 function in neurons (*10*, *12*). Considering the high neuronal expression and the established role of DAGLα in phasic endocannabinoid signaling (*15*), it was unexpected that the synaptic cannabinoid tone remained unaltered in DAGLα KO mice. Intriguingly, by inhibition of MAGL, we could unmask the presence of the DAGLα-dependent 2-AG tone at the very same synapses. This suggests the coexistence of several distinct forms of tonic cannabinoid and endocannabinoid signaling that parallels the diversity of the phasic forms of endocannabinoid signaling. The mechanistic diversity of CB_1R-dependent forms of retrograde synaptic signaling makes functional division of labor possible and demonstrates the parsimonious nature of how synapses exploit the limited number of molecular players. Considering the large-scale volumetric spread of AEA and 2-AG signaling in vivo, the AEA/2-AG tones may be ideal for the lasting control of neurotransmitter release at a circuit-wide level in association with specific physiological and pathological states (*16*–*19*, *38*, *40*).

In contrast, the NAPE-PLD/DAGLα–independent synaptic cannabinoid tone contributes to individual synaptic variability, and it is present only at perisomatically targeting, but not at dendritically targeting, CB_1R-containing GABAergic synapses (*25*). Accordingly, because CB_1Rs is involved in different synaptic mechanisms in a cell type–specific manner, it will also be important to determine how specific cell types such as excitatory neurons or astrocytes organize the nanoscale distribution of this ubiquitous GPCR.

Cannabis use disorder is becoming a major socioeconomic burden because of the steady rise in cannabis use prevalence (*78*). It is well known that CB_1Rs on GABAergic neurons play an important role in reducing hippocampal long-term potentiation, and their deletion rescues the memory impairment effects caused by acute and chronic THC administration (*79*–*81*). In this regard, it is important to emphasize that the concentration of THC in cannabis preparations is also sharply increasing (*82*). We previously found that in vivo THC exposure decreases CB_1R numbers on the surface of the axon terminals of CB_1BCs in a dose-dependent manner (*43*). In principle, this observation is an appealing example of a maladaptive molecular tolerance phenomenon, and the hypothesized concomitant synaptic defects could readily contribute to the behavioral tolerance associated with cannabis use disorder. However, in the present study, we found that a strong reduction in the total CB_1R levels on axon terminals is not necessarily accompanied by impaired phasic endocannabinoid signaling or abnormal synaptic cannabinoid tone. Considering that the nanoscale organization of intrasynaptic CB_1R signaling is a central determinant of retrograde synaptic signaling and that it remained unaffected in CB_1R HET mice despite the substantial reduction in total CB_1R levels, we reasoned that it is important to determine whether THC administration affects the nanodomain-specific CB_1R activity in the active zone. Notably, we observed a strong decrease in the intra/perisynaptic CB_1R population and in the nanoscale stoichiometry parameter after THC treatment. Consequently, the synaptic cannabinoid tone was completely absent, and synaptic variability was strongly reduced. This finding is consistent with a prior study in which acute THC exposure could eliminate CB_1R-mediated long-term synaptic depression (*83*). We also noticed that DSI was only slightly reduced. This unexpected finding further indicates that the diverse forms of retrograde cannabinoid signaling have different pathological significance, and the behavioral effects of THC will be important to study in this context in the future. Overall, our study illuminates that beyond the cell type– and subcellular compartment–specific approaches, nanodomain-restricted molecular imaging in correlation with physiological measurements are required to determine how molecular changes underlie physiological and pathological adaptive and maladaptive processes.

MATERIALS AND METHODS

Animals

Animal experiments conducted in Hungary were approved by the Hungarian Committee of the Scientific Ethics of Animal Research (license number: MÁB-2018/1), and all animal experiments were performed according to the Hungarian Act of Animal Care and Experimentation (1998, XXVIII, Section 243/1998, renewed in 40/2013), which are in accordance with the European Communities Council Directive of November 24, 1986 (86/609/EEC; Section 243/1998). Animal experiments conducted in the United States were approved by the Institutional Animal Care and Use Committee of Indiana University and conform to the National Institutes of Health Guidelines on the Care and Use of Animals. Animal experiments conducted in Italy were performed in accordance with the European legislation EU Directive 2010/63 and the National Institute of Health Guide for the Care and Use of Laboratory Animals and were approved by the Animal Ethics Committees of the University of Cagliari and by Italian Ministry of Health (authorization no. 659/2015-PR). Mice were kept under approved, specific pathogen–free laboratory conditions (12-hour light/12-hour dark cycle, 22° to 24°C, 40 to 70% humidity), and all efforts were made to minimize pain and suffering and to reduce the number of animals used. In electrophysiological, anatomical, and analytical experiments, C57Bl/6 J male mice (postnatal days 27 to 45) were used, together with strains containing genetic deletion of specific protein-coding genes: CB_1R KO (provided by A. Zimmer, University of Bonn), DAGLα KO (provided by K. Sakimura, Niigata University), NAPE-PLD KO (provided by B. Cravatt, The Skaggs Institute for Chemical Biology and Department of Chemical Physiology and The Scripps Research Institute, La Jolla, California, USA). NAPE-PLD/DAGLα double-KO mice were bred in the Medical GeneTechnology Unit of HUN-REN Institute of Experimental Medicine, under protocol PE/EA/00714-6/2022. In cases where genetically modified mice were used, their WT littermates were used for control measurements.

Acute slice preparation

Mice were decapitated under deep isoflurane anesthesia. The brains were carefully removed from the skull and transferred rapidly to ice-cold sucrose containing artificial cerebrospinal fluid (sucrose-ACSF; containing 75 mM NaCl, 75 mM sucrose, 2.5 mM KCl, 25 mM glucose, 1.25 mM NaH_2PO4, 4 mM $MgCl_2$, 0.5 mM CaCl, and 24 mM $NaHCO_3$, Sigma-Aldrich, St. Louis, MO, USA), equilibrated with 95% O_2 and 5% CO_2. All chemicals and reagents were purchased from Sigma-Aldrich, unless mentioned otherwise. Coronal hippocampal acute slices (300 μm thick) were cut with a VT-1200S Vibratome (Leica, Nussloch, Germany) (anteroposterior −1.8 to −2.8 mm from bregma) and were incubated in sucrose-ACSF for 1 hour at 34°C. Afterward, the oxygenated incubation chamber was kept at room temperature, and slices were subjected to subsequent electrophysiological, two-photon or lipid measurements.

Invitro slice electrophysiology

All electrophysiological recordings were made in a submerged recording chamber at 33°C constantly perfused with oxygenated recording ACSF solution (126 mM NaCl, 2.5 mM KCl, 10 mM glucose, 1.25 mM NaH_2PO_4, 2 mM $MgCl_2$, 2 mM $CaCl_2$, and 26 mM $NaHCO_3$). Slices were visualized with an upright Nikon Eclipse FN1 microscope equipped with infrared differential interference contrast (DIC) optics (Nikon, Tokyo, Japan).

Whole-cell patch-camp recordings were obtained from interneurons in the CA1 region of the hippocampus after visual inspection of their somatic location in the radiatum layer and their multipolar morphology under a DIC microscope. All selected cells displayed accommodating firing pattern implicating a CB_1R-positive interneuron phenotype (*84*). Recordings were carried out with borosilicate glass pipettes (0.86-mm inner diameter and 1.5-mm outer diameter with 3- to 5-megohm resistance) filled with internal solution (containing 126 mM K-gluconate, 4 mM KCl, 10 mM Hepes, 4 mM Mg–adenosine triphosphate (ATP), 0.3 mM Na_2–guanosine triphosphate (GTP), 10 mM phosphocreatine, and 8 mM biocytin; pH 7.2; 290 mOsm/kg). Pipettes were pulled with a P-1000 horizontal micropipette puller (Sutter Instrument, Novato, CA, USA). Recordings were performed using MultiClamp 700B amplifiers (Molecular Devices, San José, CA, USA). Signals were filtered at 3 kHz using a Bessel filter and digitized at 10 kHz with Digidata 1440a and 1550 analog-to-digital interface (Molecular Devices). The recorded traces were analyzed using the Clampfit 10 software (Molecular Devices). Interneuron firing patterns were studied in current-clamp configuration using current steps of 1-s duration, which ranged from −200 to +200 pA with 50-pA increments. For paired recordings, PCs were selected in the pyramidal layer of the hippocampal CA1 region and were recorded in whole-cell voltage-clamp configuration (holding potential was set to −70 mV) with internal solution containing the following: 40 mM CsCl, 90 mM K-gluconate, 1.8 mM NaCl, 1.7 mM $MgCl_2$, 3.5 mM KCl, 0.05 mM EGTA, 10 mM Hepes, 2 mM Mg-ATP, 0.4 mM Na_2-GTP, and 10 mM phosphocreatine; pH 7.2; 290 mOsm/kg). In a set of experiments, post hoc visualization of PCs was required for detailed investigation of synaptic connection between the cell pairs. Therefore, in sequential-paired experiments, in variance-mean experiments, and in correlated electrophysiological and super-resolution imaging experiments, the postsynaptic internal solution also contained Cascade Blue hydrazide (1 mg/ml), trisodium salt (Molecular Probes, Oregon, USA). Throughout paired recordings, series resistances were carefully monitored, and recordings were discarded if the series resistance changed >20% or reached 25 megaohms. Action potentials in presynaptic interneurons were elicited in current-clamp mode by injecting 2-ms-long 2-nA square pulses at 10-Hz frequency. Trains of 50 action potentials were evoked once in every minute, and effective unitary IPSC (average amplitudes include both successful events and failures) were monitored together with the number of successful events (Successes). CV for postsynaptic responses were calculated from the standard deviation of IPSC amplitudes after noise subtraction (3 min in control conditions and 3 min in the presence of the applied drug, when present) divided by the mean IPSC amplitude. DSI was induced by using a 1-s-long depolarization pulse on the PC from −70 to 0 mV. IPSCs were then compared between the pre-DSI period (2.5 s before DSI induction) and the post-DSI period (2.5 s after the end of the depolarization step). In the case of sequential recording of multiple postsynaptic cells, the experimental procedure was similar to the paired recording protocol. After successfully finding a PC that was synaptically connected to the interneuron, baseline parameters of synaptic transmission were recorded. After 10 to 15 min of recording, the capillary was carefully removed from the PC, and recordings were repeated with a subsequent postsynaptic cell.

In pharmacological experiments, AM251 (Tocris Bioscience, Bristol, UK, catalog no. 1117) was used as a CB_1R antagonist/inverse-agonist, to block CB_1R activity. To examine acute drug effects, bath ACSF was changed to drug-ACSF solution (containing 10 μM AM251) after the baseline was recorded for at least 5 to 10 min. To test the potential effects of AM251 on the nanoscale receptor distributions, slices were placed to recording ACSF for at least 10 min. Then, slices were moved to another incubation chamber that either contained 10 μM AM251 or equivalent amount of vehicle dimethyl sulfoxide (DMSO) in ACSF for 10 min. To study the effect of MAGL blockade on synaptic transmission, bath application of the MAGL inhibitor JZL184 [(4-nitrophenyl 4-[bis(1,3-benzodioxol-5-yl)(hydroxy) methyl] piperidine-1-carboxylate)] (Tocris Bioscience, Bristol, UK, catalog no. 3836) was used. In these experiments, brain slices were incubated in a drug-ACSF solution (containing 100 nM JZL184) for 40 min before recording. In each experiment, drug equivalent DMSO concentration was used as a vehicle control. Acute drug effects were quantified by averaging the postsynaptic responses to three series of 50 induced action potential trials before and 10 min after the start of drug application. In nonacute experiments, baseline values were compared between vehicle control DMSO- and drug-incubated samples.

Variance-mean analysis experiments were performed and interpreted using a simple binomial model (*85*, *86*). Briefly, 15 action potentials were evoked in the presynaptic cell with 0.3-Hz frequency in every 2 min and postsynaptic potentials were measured at the PC soma. To block CB_1R activation 1 μM AM251 was included in all bathing ACSF solutions (except during baseline recordings). After measuring baseline transmission properties on a cell pair, extracellular levels of Ca^{2+} and Mg^{2+} were changed to alter release probability (Pr) conditions. A minimum of 45 traces were required in each epoch of different Pr conditions to include a cell in the analysis. The stability of peak amplitudes in time throughout an epoch was determined by fitting a regression line to the scatter plot of IPSC amplitudes versus time. The mean Rs for the first analyzed epochs during the recordings was 18.7 ± 2.3 megohms. Because of longer recording times (40 to 90 min), if the Rs changed >45%, then the recording was discarded. All recordings were rejected when the Rs became >25 megohms. From the total of five Pr conditions per recording, stable data collection from at least four conditions were required to include a pair in the analysis. Control measurements without altering extracellular Ca^{2+} and Mg^{2+} concentrations were also conducted in parallel for similar length, to test potential time-induced changes. Comparing traces obtained during the first and the last 10 min of these experiments revealed no significant change neither in variance nor in mean amplitudes ($n = 3$ experiments). The peak amplitudes of the IPSCs and the successes were measured in a 3-ms time window after the peak of presynaptic action potential and the mean amplitude of postsynaptic responses (I) and the variances (σ^2) were calculated. Background variance (σ^2_{noise}) was measured 5 ms before the onset of the averaged postsynaptic response and was subtracted. Quantal parameters, such as quantal size (Q) and number of functional release sites (Nf) were estimated from a parabolic function fit on the variance-mean amplitude plot: $\sigma^2 = QI - I^2/Nf$, where Q can

be estimated from the initial slope and Nf*Q* can be estimated from the larger X intercept of the parabola. Pr was then calculated from the mean current using the following equation: Pr = *I*/Nf*Q*.

To derive Pr values from the ratio of successful synaptic events recorded via paired recording, Nf values of the connection are required. Previous data suggest that the number of functional release sites exceeds the anatomically identified active zones at CB_1R-expressing interneurons in the CA3 region (*86*). Quantal analysis showed a relatively low baseline Pr value (0.2 ± 0.04) with an average of three release sites per bouton (3.07 ± 0.57; n = 10 pairs) (fig. S5). Therefore, the analysis was restricted to pairs that were connected via unitary (n = 8 pairs) or two boutons (n = 1 pair) and contained only a single active zone (confocal bassoon cluster) per bouton. In case of the pair with two boutons, the connections were sufficiently apart from each other that allowed STORM imaging without bleaching (see the "STORM sample preparation and imaging" section).

After each electrophysiological recording, the sections were transferred into 4% paraformaldehyde (TAAB Ltd., Aldermaston, UK) in 0.1 M phosphate buffer (PB; pH 7.4), and fixed for 24 hours at 4°C. After fixation, slices were stored in 0.1 M PB containing 0.05% Na azide until further use.

Two-photon calcium imaging

Calcium imaging measurements were carried out on a Nikon Eclipse FN1 upright microscope, equipped with a Nikon A1R MP+ multiphoton system. Two-photon excitation was provided by a tunable Ti:Sapphire laser (Coherent Inc., Santa Clara, CA, USA), tuned to approximately 810 nm, and laser power was optimized for emission detection at different depths in the slice without causing phototoxicity. Recordings were obtained in a similar manner to electrophysiological recordings; the same solutions were used during the experiments except from the specific indicator dyes in the internal solution. K-gluconate internal solution was supplemented with morphological tracer (Alexa Fluor 594; 40 μM, Invitrogen, Thermo Fisher Scientific) and a fluorescent Ca^{2+} indicator dye (Oregon Green BAPTA 1, OGB-1, 112 μM, Invitrogen, Thermo Fisher Scientific). Recordings were carried out in a submerged recording chamber at room temperature (~23°C) constantly perfused with oxygenated ACSF solution. Current-clamp recordings were performed using MultiClamp 700B amplifier (Molecular Devices). Signals were filtered at 3 kHz using a Bessel filter and digitized at 10 kHz with Digidata 1322A (Molecular Devices). Traces were analyzed using the Clampfit 8 software (Molecular Devices). Interneurons were kept in whole-cell voltage-clamp configuration with holding potential at −70 mV. After filling the cell for approximately 60 min, the axon terminals were identified by Alexa Fluor 594. To measure the Ca^{2+} signals, green fluorescence was collected during line scans across the axon terminals. Boutons were selected in the pyramidal layer of the hippocampal CA1 region. The basal dye fluorescence (F) and the action potential generated calcium inflow (ΔF) were measured in the axon terminals of the CB_1-positive interneuron. Action potentials were evoked by somatic current injection (2-ms-long, 1300-pA square pulses). The amplitude of the Ca^{2+} transients were expressed as fractional change of the basal fluorescence $\Delta F/F$, which is proportional to the change in intracellular calcium concentration (*87*). Drug effects were measured after 10 min of AM251 application on the same axon terminals, by measuring the amplitude of the Ca^{2+} transients ($\Delta F/F$) and comparing them to control response levels. Finding the same boutons after drug application was carried out using an in-house written software. Control measurements without drug were conducted in parallel with the AM251 experiments to test potential time-induced changes in Ca^{2+} responses. The peak amplitudes of the Ca^{2+} transients decreased with 0.024 ± 0.031 $\Delta F/F$ during the ~1-hour imaging period (n = 6 cells, n = 64 boutons). Therefore, the AM251 drug effects on the peak amplitudes were corrected with this value. Comparison and analysis of calcium transients were carried out in Microsoft Excel (Redmond, WA, USA).

Immunolabeling

Supplementary data tables contain detailed information about primary and secondary antibodies used in this study (tables S1 and S2). Fluorescent immunolabeling was used to visualize single- or multiple-labeled individual cells and protein distributions in brain slices. All samples were stained in a free-floating manner in 24-well tissue culture plates (Greiner Bio-One, Mosonmagyaróvár, Hungary) in 500-μl volume on an orbital shaker (Biosan, Riga, Latvia). Protocols were fine-tuned to each experiment to provide the best quality of labeling compared to the individual antibodies and used methods.

After electrophysiological recordings, single-labeled interneuron-containing 300-μm-thick slices were washed three times in 0.1 M PB for 10 min and treated with 0.5% Triton X-100 in 0.1 M PB together with 10% normal donkey serum (NDS) in 0.1 M PB for 30 min. Slices were incubated with streptavidin conjugated to DyLight-488 for 2 hours to visualize biocytin. After washing the slices three times with 0.1 M PB for 10 min, samples were mounted on glass slides in Vectashield (H-1000, Vector Laboratories, Burlingame, CA, USA), coverslipped, and sealed with nail polish. To visualize PCs labeled with Cascade Blue along with biocytin filled interneurons, 300-μm-thick slices were washed (3 × 10 min in 0.1 M PB) and blocked with 10% NDS in 0.1 M PB for 30 min. Then, samples were incubated with a mixture of 0.5% Triton X-100, 2% NDS, and anti–Cascade Blue antibody in 0.1 M PB, which was previously incubated with an unlabeled and untreated brain slice for 1 day at 4°C, to reduce background staining. After 48 hours of incubation in primary antibody at 4°C, brain slices were washed (3 × 10 min in 0.1 M PB) and treated with a solution containing 2% NDS and fluorescent secondary antibodies for 2 hours at room temperature. Slices were washed in 0.1 M PB three times for 10 min and were mounted on glass slides in Vectashield, coverslipped, and sealed with nail polish.

After confocal imaging of cellular morphology (see the "Confocal microscopy" section), 300-μm-thick sections were first returned to PB and then embedded in 2% agarose in distilled water for resectioning. Ten- to 20-μm-thick sections were cut with a Leica VT-1000S Vibratome in 0.1 M PB. Wells were preblocked with 5% NDS in 0.1 M PB or with 1% bovine serum albumin (BSA) in 0.05 M tris-buffered saline (TBS; pH = 7.4). After extensive washing (3 × 10 min in 0.1 M PB and 3 × 15 min in 0.05 M TBS), slices were treated with a solution containing 5% NDS and 0.1% Triton X-100 in TBS for 45 min to further enhance antibody penetration. Then samples were incubated in the TBS solution of the primary antibodies overnight at room temperature. On the following day, samples were thoroughly washed (3 × 15 min in 0.05 M TBS) and incubated in the TBS solution of the fluorescently labeled secondary antibodies for 4 hours. Last, samples were washed in TBS and PB and mounted in Vectashield for microscopical imaging.

Confocal microscopy

To assess interneuron morphology, ×20 magnification z-stacks (with 1-μm step size in *z* direction) and maximal intensity z-projections of recorded cells were collected from 300-μm-thick sections on a Nikon A1R confocal scan head coupled to a Nikon Ti-E inverted microscope (Nikon Instruments, Japan) using a CFI Plan Apo VC 20× objective [numerical aperture (NA): 0.75 NA]. To visually identify close anatomical appositions of those paired recordings in which the PCs were also labeled, 60x-magnification objectives were used (CFI Plan Apo VC 60X Oil; NA: 1.4) together with appropriate Nyquist-sampling (pixel size = 0.14 μm/px, z-step = 0.125 μm) to capture high-resolution z-stacks. The same microscope and objectives were used to obtain high-resolution z-stacks of fluorescent immunostainings in hippocampus.

Cell-type identification and determining synaptic connections

Perisomatically targeting interneurons (basket cells) were separated from dendrite-targeting interneurons (dendritic cells) on the basis of their axonal arborization: the laminar distribution of boutons within the different hippocampal layers was quantified as a BDI [see detailed method in (*43*)]. Briefly, axon terminals of the interneuron were identified in the confocal maximal intensity z-projections (using ImageJ software). After specifying the pyramidal layer, the relative distance of each bouton from this layer was measured and the overall values were expressed as a BDI. BDI >1 means that the boutons of the cell were mainly accumulated in the pyramidal layer, BDI < 0.5 represented cells with boutons distributed in either str. radiatum or str. oriens. Cells with intermediate BDI value (between 0.5 and 1) were excluded from the study, except for the correlated analysis (Fig. 4), where we have included pairs with perisomatic inputs, including presynaptic basket cells ($n = 6$ pairs), and cells that exclusively targeted the soma or the close proximal dendrites of the postsynaptic PC between BDI values 0.5 and 1 ($n = 3$ pairs). The BDI together with the electrophysiological characteristics of the neurons and their immunohistochemical expression patterns of specific proteins were used for unequivocal identification of perisomatically targeting cells.

STORM sample preparation and imaging

Sections were stained (see Immunostaining) and mounted on borosilicate glass coverslips and imaged (see the "Confocal microscopy" section) following a previously described protocol (*88*). Confocal images of Cascade Blue, biocytin, bassoon and CB_1R and STORM images of CB_1R, were captured on a Nikon N-STORM system. Biocytin-filled boutons impinging on Cascade Blue–filled postsynaptic targets, identified during previous steps, were located in widefield mode. In confocal mode, z-stacks of 15 sections, with 150-nm step size were captured. Then, in STORM mode, z-stacks of 7 3D-STORM movies, 1000 cycles each, were captured using an interleaved sampling strategy, centered on the middle section of the confocal z-stack (reference plane). That is, four movies were captured with increasing distance from the coverslip, and then three movies were captured in between the planes of the first four movies. The N-STORM z-stack module was used to control TIRF angle and z-position using the optical 'perfect focus system' for each step. This recording strategy allowed highly homogenous sampling of the volume over 1000-nm thickness, as determined from inspecting the histograms of z coordinates in assembled STORM z-stack datasets (see below). Before setting the STORM acquisition range, confocal z-stacks of the bouton were inspected to ensure that the bouton is included in the recorded volume and the volume is centered (±150 nm) on the largest bassoon cluster inside the bouton, and the reference plane was adjusted as necessary. In case of multiple boutons in a section, images were captured in an order that prevented bleaching of the additional boutons, by using a rectangular field stop set tightly around the center of the imaged field of view and progressing through boutons in a direction opposite to the angle of the oblique TIRF illumination. In cases where multiple boutons were too close to be recorded in consecutive STORM z-stacks, the pair was excluded from further analysis.

Boutons from WT and CB_1R HET mice were imaged similarly as described above, with the exception that multiple CB_1R-positive boutons, selected in widefield mode at random, were imaged from each section. Boutons in the str. Pyramidale, located at ~1500 nm from the coverslip, were selected, and the field of view was centered on the selected bouton. Additional inclusion criteria were applied after inspecting the confocal z-stack: no contact with neighboring CB_1R-positive boutons (to avoid the ambiguity of detecting bouton surface), and at least one bassoon cluster within the bouton visible on the confocal image. Then, correlated confocal and 3D-STORM z stacks were recorded as described above.

STORM data processing and analysis

Confocal volume images were deconvolved using Huygens (SVI) using theoretical point spread function and the classic maximum likelihood estimation algorithm with default settings. STORM image molecule localization was performed separately on each movie of the z-stacks, using NIS Elements N-STORM (Nikon), including corrections for spherical and chromatic aberration and sample drift and fitting z positions based on a calibration curve (*88*). Because NIS Elements returns z coordinates as distance from the coverslip, to align volumetric 3D-STORM and confocal data, it is necessary to transform z coordinates to distance from the reference plane, i.e., the initial focal plane and the center plane of the confocal stack. The molecule lists from the seven (partially overlapping) STORM imaging planes were merged, and the z coordinates of LPs were clustered into seven clusters using k-means. The mean of the resulting seven centroids was used as the reference z position. The centroids and the mean were plotted against the z histogram of the merged molecule list and inspected for each file to exclude any STORM z-stacks with anomalous coordinate distribution. Last, the reference z position was subtracted from all z coordinate values.

Correlated confocal and STORM image analysis

For each imaged bouton, the confocal and STORM images of CB_1R were first aligned manually, and CB_1R LPs belonging to the bouton were selected in 2D using VividSTORM (*88*). The selected molecule list and the values of the x-y offsets for fitting the confocal and STORM datasets were saved, and all following steps were carried out using custom Python scripts. Next, the overlaid confocal and STORM volumes were plotted in three orthogonal maximum intensity projections, and the selection was further refined to exclude LPs located below or above the bouton. Then, the bassoon channel of the confocal z-stack was converted to a list of positive voxel coordinates. The stack was binarized using one third of the Otsu threshold of a region centered on the bouton (128 by 128 pixels), and positive voxels inside the bouton were selected in 3D on the orthogonal views. The included bassoon confocal voxels were density-filtered using DBSCAN

(minimum three neighbors within 200 nm). Because of the binarized images, continuous bassoon-positive voxels were treated as a single confocal cluster even if the intensity of the pixels were different. Last, a 3D convex hull was fit on density-filtered (DBSCAN, three neighbors within 100 nm) CB_1R LPs (*88*), and the distance of each CB_1R LP from the convex hull and the nearest bassoon voxel was measured. CB_1R/bassoon ratios in either cumulative or nonoverlapping distance bins were measured using the preprocessed CB_1R STORM molecule lists and confocal bassoon voxel lists. For consistency between analyses, 200-nm perisynaptic threshold distance was used for plotting Figs. 4, 6, and 7. However, the results of statistical analysis did not critically depend on the choice of distance threshold between 100 and 200 nm. Despite the nanoscale localization accuracy of CB_1Rs, due to the localization uncertainty of bassoon-positive active zones determined from confocal imaging (60-nm lateral and 150-nm axial voxel size) on one hand, and the lack of information on the exact distance dependence of CB_1R downstream signaling on the other, setting a lower perisynaptic distance threshold is not expected to further improve the accuracy of the analysis. For determining correlations of super-resolution LP data with Pr, we used the following formula, assuming three release sites per boutons with a single confocal bassoon cluster facing toward the PC: $Pr = 1 - (1- s) \wedge [1 / (n * 3)]$, where "*s*" is the ratio of successes over all trials, and "*n*" is the number of boutons in the connection.

QDs, neuronal cultures, and nanoPaint microscopy

The nanoPaint technique was previously described in detail (*45*). Red-emitting ($\lambda em = 650$ nm) CdSe/CdS/ZnS multishell QDs were synthesized, surface functionalized with a sulfobetaine vinylimidazole block copolymer ligand and thereafter bioconjugated to protein A and to rabbit anti FLAG Ab (F3040) from Sigma-Aldrich, as detailed in (*89*). Rat E17 hippocampal neuronal cultures were cultured on glass-coated poly-L-lysine coverslips in Neurobasal/B27 medium. Transfection of the plasmid FLAG-CB_1-GFP was performed at DIV8 (days in vitro) with Lipofectamine according to the manufacturer's instructions. The day of acquisition (DIVs) 18 to 28), the coverslip was mounted on a Ludin chamber inserted in a mini-incubator containing a videomicroscopy buffer and maintained at 37°C. The bioconjugated anti-FLAG-QDs were added to the medium and single-particle tracking acquisitions were obtained with a Nikon Eclipse Ti inverted microscope (Nikon Instruments) equipped with an Apo TIRF 100 × H 1.49 objective. Images were acquired with an iXon3 back-illuminated electron-multiplying charge-coupled device camera (Andor, Oxford Instruments) at 67 Hz.

nanoPaint data analysis

Video microscopy images were processed with the ThunderSTORM ImageJ plugin from the Fiji software (ImageJ). This plugin was used for the localization of single particles as well as for image reconstructions in which regions of interest were selected for synapses and axons according to morphological criteria. For trajectory analyses, the individual localizations were linked to trajectories using a homemade script written in RStudio using a cutoff of 750 nm for trajectories of two consecutive acquisitions frames. Ripley's function was calculated with the spatstat package in RStudio.

Liquid chromatography–tandem mass spectrometry

Acute hippocampal slices were prepared and treated as described before for electrophysiological experiments. Animals were housed, and brain slices were prepared in the same manner and at the same time of the day, to reduce biological variability in endocannabinoid levels. After the 1-hour regenerating incubation in sucrose-ACSF, hippocampal sections were transferred to holding chambers (for baseline lipid level measurements) containing oxygenated ACSF or to treatment chambers (for pharmacological experiments) at room temperature, containing oxygenated ACSF supplemented with 100 nM JZL184 or DMSO only (vehicle). In each chamber, five 300-μm-thick dorsal and ventral hippocampal sections of an individual animal were treated for 40 min. To further reduce potential variability, slices were collected in an alternate manner from the left and right hemispheres and were pooled into a single measured sample after pharmacological treatment. Thus, endocannabinoid levels were always compared between two hippocampal tissue samples derived from an individual animal, with the tissue being treated by either an enzyme inhibitor or its corresponding vehicle control. After pharmacological treatment, the hippocampal samples were frozen in liquid nitrogen and stored at −70°C until the measurement of endocannabinoid levels by liquid chromatography–tandem mass spectrometry.

Sample preparation for chromatography started with tissue incubation on ice for 30 min in 1 ml of methanol [high-performance liquid chromatography (HPLC)–grade, Merck, Darmstadt, Germany] containing the deuterated internal standards 2-arachidonoylglycerol-d5 (100 ng/ml; Cayman Chemicals) and arachidonoylethanolamide-d4 (1 ng/ml, Cayman Chemicals). After ultrasonic homogenization, samples were centrifuged on an Eppendorf mini-Spin microtube centrifuge at 13,400 rpm for 15 min. The supernatant was transferred into a plastic tube and was diluted with 3 ml of ultrapure water. The samples were subjected to solid-phase extraction (SPE) sample clean-up according to the following protocol. First, the SPE cartridges (SUPELCO Discovery DSC-18 1-ml tubes, 100 mg, Sigma-Aldrich) were conditioned with 2 ml of methanol and 2 ml of ultrapure water. Diluted samples were loaded onto the SPE columns (~0.5 ml/min flow rate), and consecutive washing steps were carried out by percolating 2 ml of ultrapure water and 2 ml of methanol/water (50:50, v/v%) through the sorbent material. Elution was performed with 0.7 ml of methanol. Eluates were diluted to initial HPLC eluent composition with 10 mM ammonium formate solution (Riedel-de Haën, Seelze, Germany).

To measure endocannabinoid levels, we used a PerkinElmer Life and Analytical Sciences HPLC Series 200 system (PerkinElmer, Waltham, MA, USA), which was coupled to an Applied Biosystems/Sciex 4000 QTRAP triple quadrupole/linear ion trap tandem mass spectrometer (Applied Biosystems, Foster City, CA, USA) operated in positive electrospray ionization mode. The electrospray ionization–positive ion source parameters were set as follows: curtain gas, 10; ionspray voltage, 5000 V; temperature, 500°C; collisionally activated dissociation gas, medium; gas-1, 50; gas-2, 40. Chromatographic separation was achieved with a Phenomenex Kinetex C18 column (50 mm by 3.00 mm, 2.6 μm, 100 Å, Phenomenex, Torrance, CA, USA) using methanol and 10 mM ammonium formate as elution solvents at a flow rate of 500 μl/min. The injection volume was 50 μl. The initial eluent condition was 80% methanol–20% buffer that was increased to 85% organic phase for 3 min and then further elevated to 95% for 2 min and was kept at this condition for 2 min. Afterward, the column was equilibrated to the initial condition. Analytes were detected in multiple reaction monitoring (MRM) mode at the following ion transitions and parameter settings:

(i) 2-AG, MRM transition [mass/charge ratio (m/z) 379.4 → 287.2, m/z 379.4 → 91.1], declustering potential (81 V), collision energy (23 V, 81 V), cell exit potential (10 V, 8 V); (ii) 2-AG-d5, MRM transition (m/z 384.4 → 287.2, 384.4 → 91.1), declustering potential (81 V), collision energy (23 V, 81 V), cell exit potential (10 V, 8 V); (iii) arachidonoylethanolamide, MRM transition (m/z 348.4 → 62.1, 348.4 → 90.9), declustering potential (51 V), collision energy (43 V, 63 V), cell exit potential (4 V, 8 V); and (iv) arachidonoylethanolamide-d4, MRM transition (m/z 352.4 → 66.0, 352.4 → 91.2), declustering potential (81 V), collision energy (41 V, 77 V), cell exit potential (6 V). The peak areas were determined with Analyst 1.4.2. software. The quantity of the analytes was calculated by comparing their peak areas with those of the deuterated internal standards and normalized to the sample weight.

Western blot experiments

Twenty-five– to 30-day-old male CB_1R WT, HET, and KO mice were euthanized by cervical dislocation and decapitated. Three mice were used for each genotype. After sectioning, 300-µm-thick slices containing hippocampi were collected. From these slices, three pairs of hippocampi (including the cortex) were isolated for further experiments during constant cooling with dry ice. Then, the tissue was homogenized in homogenization buffer (HB; 10 mM Hepes, 10 mM KCl, 1 mM $MgCl_2$, 1 mM dithiothreitol, and 1 Roche complete protease inhibitor pill/10 ml). After spinning at 3500 rpm for 5 min at 4°C, the pellets were discarded as the nuclear fraction. The supernatants were collected and span at 15,000 rpm for 1 hour at 4°C, then the new supernatants were gathered as cytoplasmic and the pellets as membrane fractions. The pellets were resuspended in 150 µl of HB, and then 1% (v/v) Triton X-100 was added to both the cytoplasmic and membrane fractions. The samples were vortexed and left on ice for 30 min, then span at 15,000 rpm for 10 min at 4°C. The fractions were aliquoted and the concentrations were analyzed by Coomassie Plus protein assay reagent (Thermo Fisher Scientific). Purified membrane protein (40 µg) was denaturated with 4x Laemmli Sample Buffer (Bio-Rad) for 10 min at 37°C. Samples were run on 13.5% polyacrylamide gel at 60 V for 30 min, then at 200 V for 2 hours at 4°C, and transferred onto nitrocellulose membranes (Bio-Rad) at 300 mA for 2 hours at 4°C. The transfer was verified with Ponceau S stain (Amresco) and the membranes were washed twice with TBS containing 0.05% Tween 20 (TBST), then blocked with 5% skimmed milk powder (TUTTI Élelmiszeripari Kft.) in TBST for 1 hour at room temperature. After the membranes were washed twice in TBST, the blots were incubated in primary antibodies (rabbit polyclonal CB_1R antibody, 1/4000 diluted in blocking solution overnight at 4°C. Then, the membranes were washed twice in TBST and incubated in horseradish peroxidase (HRP)–linked anti-rabbit secondary antibody solution (Cell Signaling, 1/1000) for 1 hour at room temperature. The blots were washed twice with TBST and tris buffer, then incubated in enhanced chemiluminescent substrate solution (Thermo Fisher Scientific SuperSignal West Dura Extended Duration Substrate) according to the manufacturer's instructions. The luminescence was imaged with Chemi Genius 2 Bio Imaging System (Syngene). The blot was then reexposed with another antibody, mouse Na^+- and K^+-dependent adenosine triphosphatase (Merck Millipore, 1/4000) and the incubation steps were repeated with HRP-linked anti-mouse secondary antibody solution (Cell Signaling, 1/1000). Gray value calculation and Western visualization were done using Adobe Photoshop.

Chronic drug treatment

Animals were grouped in a randomized manner and treated either with THC or its vehicle (1% ethanol, 2% Tween 80, and saline) intraperitoneally at a dose of 10 mg/kg (intraperitoneal injection volume of 10 ml/kg) twice a day for 6.5 days. THC (THC-Pharm GmbH, Germany) was dissolved in a solution containing 1% ethanol, 2% Tween 80, and saline. The chronic treatment regimen with a dose of 10 mg/kg was shown to induce behavioral tolerance in mice (*90*, *91*). From all the experimental groups, 24 hours after the last THC or vehicle injection, mice were anesthetized with isoflurane, and acute slices were cut to perform electrophysiological recordings and subsequent confocal and STORM imaging as described above. For the duration of the experiment and analysis, samples were processed by experimenters blinded to treatment.

Statistical analysis and quantification

The obtained data from the different experiments were statistically analyzed using GraphPad Prism 10 software (San Diego, CA, USA). Sample sizes were estimated on the basis of previous experience and are similar to those generally applied and accepted in the field. Normality of the data was checked by Shapiro-Wilk test or Kolmogorov-Smirnov normality test (depending on sample numbers). If data showed normal distribution, paired or unpaired t test was used for analysis; when data did not show normal distribution, nonparametric Wilcoxon's signed-rank test or Mann-Whitney U test was used for paired and unpaired data, respectively. Correlation between two variables were tested using either Pearson's correlation or Spearman's rank-order correlation, depending on the normality distribution of the dataset. Comparison and statistical analysis of baseline conditions and drug treatment effects on multiple genotypes were conducted via two-way analysis of variance (ANOVA) with repeated measures. The statistical tests used in each experiment are described in their respective figure legend together with detailed P values and sample size ("n"). Data presented as means ± SEM unless otherwise stated. Throughout the study, differences were considered statistically significant when $^*P \leq 0.05$, $^{**}P \leq 0.01$, $^{***}P \leq 0.001$. In case of calcium imaging measurements, where one experiment consisted at least 15 boutons per cell, boutons from different animals were pooled if there was no significant difference between the baseline values of animals or cells of any group (Kruskal-Wallis test, $P > 0.05$).

Graphs were generated using GraphPad Prism 10 software. Neurolucida software (MBF Bioscience, Delft, The Netherlands) was used to create reconstructions from individually labeled cells. For figure preparation, Adobe Photoshop and Illustrator (Adobe Inc., San Jose, CA, USA) were used, where all images were treated in the same manner for all groups or genotypes.

Supplementary Materials

This PDF file includes:

Figs. S1 to S8
Tables S1 and S2
Legend for data S1

Other Supplementary Material for this manuscript includes the following:

Data S1

REFERENCES AND NOTES

1. T. Biederer, P. S. Kaeser, T. A. Blanpied, Transcellular Nanoalignment of Synaptic Function. *Neuron* **96**, 680–696 (2017).

2. D. Choquet, M. Sainlos, J.-B. Sibarita, Advanced imaging and labelling methods to decipher brain cell organization and function. *Nat. Rev. Neurosci.* **22**, 237–255 (2021).
3. A.-H. Tang, H. Chen, T. P. Li, S. R. Metzbower, H. D. MacGillavry, T. A. Blanpied, A trans-synaptic nanocolumn aligns neurotransmitter release to receptors. *Nature* **536**, 210–214 (2016).
4. K. C. Crosby, S. E. Gookin, J. D. Garcia, K. M. Hahm, M. L. Dell'Acqua, K. R. Smith, Nanoscale subsynaptic domains underlie the organization of the inhibitory synapse. *Cell Rep.* **26**, 3284–3297.e3 (2019).
5. M. Hruska, N. Henderson, S. J. Le Marchand, H. Jafri, M. B. Dalva, Synaptic nanomodules underlie the organization and plasticity of spine synapses. *Nat. Neurosci.* **21**, 671–682 (2018).
6. A. M. Ramsey, A.-H. Tang, T. A. LeGates, X.-Z. Gou, B. E. Carbone, S. M. Thompson, T. Biederer, T. A. Blanpied, Subsynaptic positioning of AMPARs by LRRTM2 controls synaptic strength. *Sci. Adv.* **7**, eabf3126 (2021).
7. T. Branco, K. Staras, The probability of neurotransmitter release: Variability and feedback control at single synapses. *Nat. Rev. Neurosci.* **10**, 373–383 (2009).
8. D. M. Lovinger, Y. Mateo, K. A. Johnson, S. A. Engi, M. Antonazzo, J. F. Cheer, Local modulation by presynaptic receptors controls neuronal communication and behaviour. *Nat. Rev. Neurosci.* **23**, 191–203 (2022).
9. Y. Zhang, K. Chen, S. A. Sloan, M. L. Bennett, A. R. Scholze, S. O'Keeffe, H. P. Phatnani, P. Guarnieri, C. Caneda, N. Ruderisch, S. Deng, S. A. Liddelow, C. Zhang, R. Daneman, T. Maniatis, B. A. Barres, J. Q. Wu, An RNA-sequencing transcriptome and splicing database of glia, neurons, and vascular cells of the cerebral cortex. *J. Neurosci.* **34**, 11929–11947 (2014).
10. A. Neu, C. Földy, I. Soltesz, Postsynaptic origin of CB1-dependent tonic inhibition of GABA release at cholecystokinin-positive basket cell to pyramidal cell synapses in the CA1 region of the rat hippocampus. *J. Physiol.* **578**, 233–247 (2007).
11. A. Losonczy, Á. A. Biró, Z. Nusser, Persistently active cannabinoid receptors mute a subpopulation of hippocampal interneurons. *Proc. Natl. Acad. Sci. U.S.A.* **101**, 1362–1367 (2004).
12. C. Földy, R. C. Malenka, T. C. Südhof, Autism-associated neuroligin-3 mutations commonly disrupt tonic endocannabinoid signaling. *Neuron* **78**, 498–509 (2013).
13. H. E. Speed, M. Kouser, Z. Xuan, J. M. Reimers, C. F. Ochoa, N. Gupta, S. Liu, C. M. Powell, Autism-associated insertion mutation (InsG) of Shank3 Exon 21 causes impaired synaptic transmission and behavioral deficits. *J. Neurosci.* **35**, 9648–9665 (2015).
14. H.-C. Lu, K. Mackie, An introduction to the endogenous cannabinoid system. *Biol. Psychiatry* **79**, 516–525 (2016).
15. A. Tanimura, M. Yamazaki, Y. Hashimotodani, M. Uchigashima, S. Kawata, M. Abe, Y. Kita, K. Hashimoto, T. Shimizu, M. Watanabe, K. Sakimura, M. Kano, The endocannabinoid 2-arachidonoylglycerol produced by diacylglycerol lipase α mediates retrograde suppression of synaptic transmission. *Neuron* **65**, 320–327 (2010).
16. Y. Hashimotodani, T. Ohno-Shosaku, M. Kano, Presynaptic monoacylglycerol lipase activity determines basal endocannabinoid tone and terminates retrograde endocannabinoid signaling in the hippocampus. *J. Neurosci.* **27**, 1211–1219 (2007).
17. J. Kim, B. E. Alger, Reduction in endocannabinoid tone is a homeostatic mechanism for specific inhibitory synapses. *Nat. Neurosci.* **13**, 592–600 (2010).
18. D. J. Marcus, G. Bedse, A. D. Gaulden, J. D. Ryan, V. Kondev, N. D. Winters, L. E. Rosas-Vidal, M. Altemus, K. Mackie, F. S. Lee, E. Delpire, S. Patel, Endocannabinoid signaling collapse mediates stress-induced amygdalo-cortical strengthening. *Neuron* **105**, 1062–1076.e6 (2020).
19. G. N. Petrie, G. Balsevich, T. Füzesi, R. J. Aukema, W. P. F. Driever, M. van der Stelt, J. S. Bains, M. N. Hill, Disruption of tonic endocannabinoid signalling triggers cellular, behavioural and neuroendocrine responses consistent with a stress response. *Br. J. Pharmacol.* **180**, 3146–3159 (2023).
20. S. Oubraim, R. Wang, K. A. Hausknecht, R.-Y. Shen, S. Haj-Dahmane, Tonic endocannabinoid signaling gates synaptic plasticity in dorsal raphe nucleus serotonin neurons through peroxisome proliferator-activated receptors. *Front. Pharmacol.* **12**, 691219 (2021).
21. H. Sharir, M. E. Abood, Pharmacological characterization of GPR55, a putative cannabinoid receptor. *Pharmacol. Ther.* **126**, 301–313 (2010).
22. R. Baur, J. Gertsch, E. Sigel, The cannabinoid CB1 receptor antagonists rimonabant (SR141716) and AM251 directly potentiate GABAA receptors. *Br. J. Pharmacol.* **165**, 2479–2484 (2012).
23. K. A. Seely, L. K. Brents, L. N. Franks, M. Rajasekaran, S. M. Zimmerman, W. E. Fantegrossi, P. L. Prather, AM-251 and rimonabant act as direct antagonists at mu-opioid receptors: Implications for opioid/cannabinoid interaction studies. *Neuropharmacology* **63**, 905–915 (2012).
24. E. C. Rosenberg, S. Chamberland, M. Bazelot, E. R. Nebet, X. Wang, S. McKenzie, S. Jain, S. Greenhill, M. Wilson, N. Marley, A. Salah, S. Bailey, P. H. Patra, R. Rose, N. Chenouard, S. D. Sun, D. Jones, G. Buzsáki, O. Devinsky, G. Woodhall, H. E. Scharfman, B. J. Whalley, R. W. Tsien, Cannabidiol modulates excitatory-inhibitory ratio to counter hippocampal hyperactivity. *Neuron* **111**, 1282–1300.e8 (2023).
25. S.-H. Lee, M. Ledri, B. Tóth, I. Marchionni, C. M. Henstridge, B. Dudok, K. Kenesei, L. Barna, S. I. Szabó, T. Renkecz, M. Oberoi, M. Watanabe, C. L. Limoli, G. Horvai, I. Soltesz, I. Katona, Multiple forms of endocannabinoid and endovanilloid signaling regulate the tonic control of GABA release. *J. Neurosci.* **35**, 10039–10057 (2015).
26. N. Lenkey, T. Kirizs, N. Holderith, Z. Máté, G. Szabó, E. S. Vizi, N. Hájos, Z. Nusser, Tonic endocannabinoid-mediated modulation of GABA release is independent of the CB1 content of axon terminals. *Nat. Commun.* **6**, 6557 (2015).
27. K. R. Jensen, C. Berthoux, K. Nasrallah, P. E. Castillo, Multiple cannabinoid signaling cascades powerfully suppress recurrent excitation in the hippocampus. *Proc. Natl. Acad. Sci. U.S.A.* **118**, e2017590118 (2021).
28. I. del Pino, J. R. Brotons-Mas, A. Marques-Smith, A. Marighetto, A. Frick, O. Marín, B. Rico, Abnormal wiring of CCK^+ basket cells disrupts spatial information coding. *Nat. Neurosci.* **20**, 784–792 (2017).
29. X. Sun, M. J. Bernstein, M. Meng, S. Rao, A. T. Sørensen, L. Yao, X. Zhang, P. O. Anikeeva, Y. Lin, Functionally distinct neuronal ensembles within the memory engram. *Cell* **181**, 410–423.e17 (2020).
30. E. L. Yap, N. L. Pettit, C. P. Davis, M. A. Nagy, D. A. Harmin, E. Golden, O. Dagliyan, C. Lin, S. Rudolph, N. Sharma, E. C. Griffith, C. D. Harvey, M. E. Greenberg, Bidirectional perisomatic inhibitory plasticity of a Fos neuronal network. *Nature* **590**, 115–121 (2021).
31. D. Robbe, S. M. Montgomery, A. Thome, P. E. Rueda-Orozco, B. L. McNaughton, G. Buzsaki, Cannabinoids reveal importance of spike timing coordination in hippocampal function. *Nat. Neurosci.* **9**, 1526–1533 (2006).
32. M. K. Grauel, M. Maglione, S. Reddy-Alla, C. G. Willmes, M. M. Brockmann, T. Trimbuch, T. Rosenmund, M. Pangalos, G. Vardar, A. Stumpf, A. M. Walter, B. R. Rost, B. J. Eickholt, V. Haucke, D. Schmitz, S. J. Sigrist, C. Rosenmund, Rim-binding protein 2 regulates release probability by fine-tuning calcium channel localization at murine hippocampal synapses. *Proc. Natl. Acad. Sci. U.S.A.* **113**, 11615–11620 (2016).
33. H. L. Atwood, S. Karunanithi, Diversification of synaptic strength: Presynaptic elements. *Nat. Rev. Neurosci.* **3**, 497–516 (2002).
34. C. Leterrier, J. Lainé, M. Darmon, H. Boudin, J. Rossier, Z. Lenkei, Constitutive activation drives compartment-selective endocytosis and axonal targeting of type 1 cannabinoid receptors. *J. Neurosci.* **26**, 3141–3153 (2006).
35. M. Maroso, G. G. Szabo, H. K. Kim, A. Alexander, A. D. Bui, S.-H. Lee, B. Lutz, I. Soltesz, Cannabinoid control of learning and memory through HCN channels. *Neuron* **89**, 1059–1073 (2016).
36. J. A. Brock, A. Thomazeau, A. Watanabe, S. S. Y. Li, P. J. Sjöström, A practical guide to using CV analysis for determining the locus of synaptic plasticity. *Front. Synaptic Neurosci.* **12**, 11 (2020).
37. Y. Okamoto, J. Morishita, K. Tsuboi, T. Tonai, N. Ueda, Molecular characterization of a phospholipase D generating anandamide and its congeners. *J. Biol. Chem.* **279**, 5298–5305 (2004).
38. E. D. Mock, M. Mustafa, O. Gunduz-Cinar, R. Cinar, G. N. Petrie, V. Kantae, X. Di, D. Ogasawara, Z. V. Varga, J. Paloczi, C. Miliano, G. Donvito, A. C. M. van Esbroeck, A. M. F. van der Gracht, I. Kotsogianni, J. K. Park, A. Martella, T. van der Wel, M. Soethoudt, M. Jiang, T. J. Wendel, A. P. A. Janssen, A. T. Bakker, C. M. Donovan, L. I. Castillo, B. I. Florea, J. Wat, H. van den Hurk, M. Wittwer, U. Grether, A. Holmes, C. A. A. van Boeckel, T. Hankemeier, B. F. Cravatt, M. W. Buczynski, M. N. Hill, P. Pacher, A. H. Lichtman, M. van der Stelt, Discovery of a NAPE-PLD inhibitor that modulates emotional behavior in mice. *Nat. Chem. Biol.* **16**, 667–675 (2020).
39. T. Bisogno, F. Howell, G. Williams, A. Minassi, M. G. Cascio, A. Ligresti, I. Matias, A. Schiano-moriello, P. Paul, E. Williams, U. Gangadharan, C. Hobbs, V. Di Marzo, P. Doherty, Cloning of the first sn1-DAG lipases points to the spatial and temporal regulation of endocannabinoid signaling in the brain. *J. Cell Biol.* **163**, 463–468 (2003).
40. J. S. Farrell, R. Colangeli, A. Dong, A. G. George, K. Addo-Osafo, P. J. Kingsley, M. Morena, M. D. Wolff, B. Dudok, K. He, T. A. Patrick, K. A. Sharkey, S. Patel, L. J. Marnett, M. N. Hill, Y. Li, G. C. Teskey, I. Soltesz, In vivo endocannabinoid dynamics at the timescale of physiological and pathological neural activity. *Neuron* **109**, 2398–2403.e4 (2021).
41. W. I. Weis, B. K. Kobilka, The molecular basis of G protein–Coupled receptor activation. *Annu. Rev. Biochem.* **87**, 897–919 (2018).
42. B. G. Wilhelm, S. Mandad, S. Truckenbrodt, K. Kröhnert, C. Schäfer, B. Rammner, S. J. Koo, G. A. Claßen, M. Krauss, V. Haucke, H. Urlaub, S. O. Rizzoli, Composition of isolated synaptic boutons reveals the amounts of vesicle trafficking proteins. *Science* **344**, 1023–1028 (2014).
43. B. Dudok, L. Barna, M. Ledri, S. I. Szabó, E. Szabadits, B. Pintér, S. G. Woodhams, C. M. Henstridge, G. Y. Balla, R. Nyilas, C. Varga, S.-H. Lee, M. Matolcsi, J. Cervenak, I. Kacskovics, M. Watanabe, C. Sagheddu, M. Melis, M. Pistis, I. Soltesz, I. Katona, Cell-specific STORM super-resolution imaging reveals nanoscale organization of cannabinoid signaling. *Nat. Neurosci.* **18**, 75–86 (2015).
44. L. Mikasova, L. Groc, D. Choquet, O. J. Manzoni, Altered surface trafficking of presynaptic cannabinoid type 1 receptor in and out synaptic terminals parallels receptor desensitization. *Proc. Natl. Acad. Sci. U.S.A.* **105**, 18596–18601 (2008).

45. M. Tasso, T. Pons, N. Lequeux, J. Nguyen, Z. Lenkei, D. Zala, NanoPaint: A tool for rapid and dynamic imaging of membrane structural plasticity at the nanoscale. *Small* **15**, e1902796 (2019).
46. J. Del Castillo, B. Katz, Quantal components of the end-plate potential. *J. Physiol.* **124**, 560–573 (1954).
47. T. C. Südhof, The molecular machinery of neurotransmitter release (Nobel Lecture). *Angew. Chemie Int. Ed.* **53**, 12696–12717 (2014).
48. J. Rizo, Molecular mechanisms underlying neurotransmitter release. *Annu. Rev. Biophys.* **51**, 377–408 (2022).
49. L. Aitchison, J. Jegminat, J. A. Menendez, J.-P. Pfister, A. Pouget, P. E. Latham, Synaptic plasticity as Bayesian inference. *Nat. Neurosci.* **24**, 565–571 (2021).
50. D. W. Volk, D. A. Lewis, The role of endocannabinoid signaling in cortical inhibitory neuron dysfunction in schizophrenia. *Biol. Psychiatry* **79**, 595–603 (2016).
51. B. Dudok, P. M. Klein, E. Hwaun, B. R. Lee, Z. Yao, O. Fong, J. C. Bowler, S. Terada, F. T. Sparks, G. G. Szabo, J. S. Farrell, J. Berg, T. L. Daigle, B. Tasic, J. Dimidschstein, G. Fishell, A. Losonczy, H. Zeng, I. Soltesz, Alternating sources of perisomatic inhibition during behavior. *Neuron* **109**, 997–1012.e9 (2021).
52. C. Földy, A. Neu, M. V. Jones, I. Soltesz, Presynaptic, activity-dependent modulation of cannabinoid type 1 receptor-mediated inhibition of GABA release. *J. Neurosci.* **26**, 1465–1469 (2006).
53. A. Busquets-Garcia, J. Bains, G. Marsicano, CB1 receptor signaling in the brain: Extracting specificity from ubiquity. *Neuropsychopharmacology* **43**, 4–20 (2018).
54. M. A. Böhme, A. W. McCarthy, A. T. Grasskamp, C. B. Beuschel, P. Goel, M. Jusyte, D. Laber, S. Huang, U. Rey, A. G. Petzoldt, M. Lehmann, F. Göttfert, P. Haghighi, S. W. Hell, D. Owald, D. Dickman, S. J. Sigrist, A. M. Walter, Rapid active zone remodeling consolidates presynaptic potentiation. *Nat. Commun.* **10**, 1085 (2019).
55. Z. L. Newman, D. Bakshinskaya, R. Schultz, S. J. Kenny, S. Moon, K. Aghi, C. Stanley, N. Marnani, R. Li, J. Bleier, K. Xu, E. Y. Isacoff, Determinants of synapse diversity revealed by super-resolution quantal transmission and active zone imaging. *Nat. Commun.* **13**, 229 (2022).
56. S. Prokop, P. Ábrányi-Balogh, B. Barti, M. Vámosi, M. Zöldi, L. Barna, G. M. Urbán, A. D. Tóth, B. Dudok, A. Egyed, H. Deng, G. M. Leggio, L. Hunyady, M. van der Stelt, G. M. Keserű, I. Katona, PharmacoSTORM nanoscale pharmacology reveals cariprazine binding on Islands of Calleja granule cells. *Nat. Commun.* **12**, 6505 (2021).
57. G. G. Szabó, N. Lenkey, N. Holderith, T. Andrási, Z. Nusser, N. Hájos, Presynaptic calcium channel inhibition underlies CB1 cannabinoid receptor-mediated suppression of GABA release. *J. Neurosci.* **34**, 7958–7963 (2014).
58. H. A. Dunn, C. Orlandi, K. A. Martemyanov, Beyond the ligand: Extracellular and transcellular G protein–Coupled receptor complexes in physiology and pharmacology. *Pharmacol. Rev.* **71**, 503–519 (2019).
59. Y. Han, R. Cao, L. Qin, L. Y. Chen, A.-H. Tang, T. C. Südhof, B. Zhang, Neuroligin-3 confines AMPA receptors into nanoclusters, thereby controlling synaptic strength at the calyx of Held synapses. *Sci. Adv.* **8**, eabo4173 (2022).
60. M. Uchigashima, K. Konno, E. Demchak, A. Cheung, T. Watanabe, D. G. Keener, M. Abe, T. Le, K. Sakimura, T. Sasaoka, T. Uemura, Y. Imamura Kawasawa, M. Watanabe, K. Futai, Specific Neuroligin3–αNeurexin1 signaling regulates GABAergic synaptic function in mouse hippocampus. *eLife* **9**, e59545 (2020).
61. O. Durydivka, K. Mackie, J. Blahos, SGIP1 in axons prevents internalization of desensitized CB1R and modifies its function. *Front. Neurosci.* **17**, 1213094 (2023).
62. M. Dvorakova, A. Kubik-Zahorodna, A. Straiker, R. Sedlacek, A. Hajkova, K. Mackie, J. Blahos, SGIP1 is involved in regulation of emotionality, mood, and nociception and modulates in vivo signalling of cannabinoid CB 1 receptors. *Br. J. Pharmacol.* **178**, 1588–1604 (2021).
63. C. Njoo, N. Agarwal, B. Lutz, R. Kuner, The cannabinoid receptor CB1 interacts with the WAVE1 complex and plays a role in actin dynamics and structural plasticity in neurons. *PLoS Biol.* **13**, e1002286 (2015).
64. C. Costas-Insua, E. Moreno, I. B. Maroto, A. Ruiz-Calvo, R. Bajo-Grañeras, D. Martín-Gutiérrez, R. Diez-Alarcia, M. T. Vilaró, R. Cortés, N. García-Font, R. Martín, M. Espina, J. Botta, S. Ginés, P. J. McCormick, J. Sánchez-Prieto, I. Galve-Roperh, G. Mengod, L. Urigüen, G. Marsicano, L. Bellocchio, E. I. Canela, V. Casadó, I. Rodríguez-Crespo, M. Guzmán, Identification of BiP as a CB 1 receptor-interacting protein that fine-tunes cannabinoid signaling in the mouse brain. *J. Neurosci.* **41**, 7924–7941 (2021).
65. I. B. Maroto, C. Costas-Insua, C. Berthoux, E. Moreno, A. Ruiz-Calvo, C. Montero-Fernández, A. Macías-Camero, R. Martín, N. García-Font, J. Sánchez-Prieto, G. Marsicano, L. Bellocchio, E. I. Canela, V. Casadó, I. Galve-Roperh, Á. Núñez, D. Fernández de Sevilla, I. Rodríguez-Crespo, P. E. Castillo, M. Guzmán, Control of a hippocampal recurrent excitatory circuit by cannabinoid receptor-interacting protein Gap43. *Nat. Commun.* **14**, 2303 (2023).
66. L. C. Blume, K. Eldeeb, C. E. Bass, D. E. Selley, A. C. Howlett, Cannabinoid receptor interacting protein (CRIP1a) attenuates CB1R signaling in neuronal cells. *Cell. Signal.* **27**, 716–726 (2015).
67. L. C. Blume, S. Leone-Kabler, D. J. Luessen, G. S. Marrs, E. Lyons, C. E. Bass, R. Chen, D. E. Selley, A. C. Howlett, Cannabinoid receptor interacting protein suppresses agonist-driven CB1 receptor internalization and regulates receptor replenishment in an agonist-biased manner. *J. Neurochem.* **139**, 396–407 (2016).
68. S. Guggenhuber, A. Alpar, R. Chen, N. Schmitz, M. Wickert, T. Mattheus, A. E. Harasta, M. Purrio, N. Kaiser, M. R. Elphick, K. Monory, W. Kilb, H. J. Luhmann, T. Harkany, B. Lutz, M. Klugmann, Cannabinoid receptor-interacting protein Crip1a modulates CB1 receptor signaling in mouse hippocampus. *Brain Struct. Funct.* **221**, 2061–2074 (2016).
69. A. B. Roland, A. Ricobaraza, D. Carrel, B. M. Jordan, F. Rico, A. Simon, M. Humbert-Claude, J. Ferrier, M. H. McFadden, S. Scheuring, Z. Lenkei, Cannabinoid-induced actomyosin contractility shapes neuronal morphology and growth. *eLife* **3**, e03159 (2014).
70. C. Patzke, J. Dai, M. M. Brockmann, Z. Sun, P. Fenske, C. Rosenmund, T. C. Südhof, Cannabinoid receptor activation acutely increases synaptic vesicle numbers by activating synapsins in human synapses. *Mol. Psychiatry* **26**, 6253–6268 (2021).
71. D. Jullié, M. Stoeber, J. B. Sibarita, H. L. Zieger, T. M. Bartol, S. Arttamangkul, T. J. Sejnowski, E. Hosy, M. von Zastrow, A discrete presynaptic vesicle cycle for neuromodulator receptors. *Neuron* **105**, 663–677.e8 (2020).
72. Z. Hussain, T. Uyama, K. Tsuboi, N. Ueda, Mammalian enzymes responsible for the biosynthesis of N-acylethanolamines. *Biochim. Biophys. Acta - Mol. Cell Biol. Lipids* **1862**, 1546–1561 (2017).
73. Z. I. László, Z. Lele, M. Zöldi, V. Miczán, F. Mógor, G. M. Simon, K. Mackie, I. Kacskovics, B. F. Cravatt, I. Katona, ABHD4-dependent developmental anoikis safeguards the embryonic brain. *Nat. Commun.* **11**, 4363 (2020).
74. W. R. Marrs, J. L. Blankman, E. A. Horne, A. Thomazeau, Y. H. Lin, J. Coy, A. L. Bodor, G. G. Muccioli, S. S. J. Hu, G. Woodruff, S. Fung, M. Lafourcade, J. P. Alexander, J. Z. Long, W. Li, C. Xu, T. Möller, K. MacKie, O. J. Manzoni, B. F. Cravatt, N. Stella, The serine hydrolase ABHD6 controls the accumulation and efficacy of 2-AG at cannabinoid receptors. *Nat. Neurosci.* **13**, 951–957 (2010).
75. J. Schwenk, D. Baehrens, A. Haupt, W. Bildl, S. Boudkkazi, J. Roeper, B. Fakler, U. Schulte, Regional diversity and developmental dynamics of the AMPA-receptor proteome in the mammalian brain. *Neuron* **84**, 41–54 (2014).
76. A. C. M. van Esbroeck, V. Kantae, X. Di, T. van der Wel, H. den Dulk, A. F. Stevens, S. Singh, A. T. Bakker, B. I. Florea, N. Stella, H. S. Overkleeft, T. Hankemeier, M. van der Stelt, Identification of α,β-Hydrolase Domain Containing Protein 6 as a Diacylglycerol Lipase in Neuro-2a Cells. *Front. Mol. Neurosci.* **12**, 286 (2019).
77. A. Viader, D. Ogasawara, C. M. Joslyn, M. Sanchez-Alavez, S. Mori, W. Nguyen, B. Conti, B. F. Cravatt, A chemical proteomic atlas of brain serine hydrolases identifies cell type-specific pathways regulating neuroinflammation. *eLife* **5**, e12345 (2016).
78. J. M. N. Ferland, Y. L. Hurd, Deconstructing the neurobiology of cannabis use disorder. *Nat. Neurosci.* **23**, 600–610 (2020).
79. K. Monory, M. Polack, A. Remus, B. Lutz, M. Korte, Cannabinoid CB1 receptor calibrates excitatory synaptic balance in the mouse hippocampus. *J. Neurosci.* **35**, 3842–3850 (2015).
80. E. Puighermanal, G. Marsicano, A. Busquets-Garcia, B. Lutz, R. Maldonado, A. Ozaita, Cannabinoid modulation of hippocampal long-term memory is mediated by mTOR signaling. *Nat. Neurosci.* **12**, 1152–1158 (2009).
81. E. Puighermanal, A. Busquets-Garcia, M. Gomis-González, G. Marsicano, R. Maldonado, A. Ozaita, Dissociation of the Pharmacological Effects of THC by mTOR Blockade. *Neuropsychopharmacology* **38**, 1334–1343 (2013).
82. S. Chandra, M. M. Radwan, C. G. Majumdar, J. C. Church, T. P. Freeman, M. A. ElSohly, New trends in cannabis potency in USA and Europe during the last decade (2008–2017). *Eur. Arch. Psychiatry Clin. Neurosci.* **269**, 5–15 (2019).
83. S. Mato, V. Chevaleyre, D. Robbe, A. Pazos, P. E. Castillo, O. J. Manzoni, A single in-vivo exposure to Δ9THC blocks endocannabinoid-mediated synaptic plasticity. *Nat. Neurosci.* **7**, 585–586 (2004).
84. S.-H. Lee, C. Foldy, I. Soltesz, Distinct endocannabinoid control of GABA release at perisomatic and dendritic synapses in the hippocampus. *J. Neurosci.* **30**, 7993–8000 (2010).
85. J. D. Clements, R. A. Silver, Unveiling synaptic plasticity: A new graphical and analytical approach. *Trends Neurosci.* **23**, 105–113 (2000).
86. A. A. Biro, N. B. Holderith, Z. Nusser, Release probability-dependent scaling of the postsynaptic responses at single hippocampal GABAergic synapses. *J. Neurosci.* **26**, 12487–12496 (2006).
87. M. Kisfali, T. Lorincz, E. S. Vizi, Comparison of $Ca2^+$ transients and $[Ca2^+]i$ in the dendrites and boutons of non-fast-spiking GABAergic hippocampal interneurons using two-photon laser microscopy and high- and low-affinity dyes. *J. Physiol.* **591**, 5541–5553 (2013).
88. L. Barna, B. Dudok, V. Miczán, A. Horváth, Z. I. László, I. Katona, Correlated confocal and super-resolution imaging by VividSTORM. *Nat. Protoc.* **11**, 163–183 (2016).
89. M. Tasso, E. Giovanelli, D. Zala, S. Bouccara, A. Fragola, M. Hanafi, Z. Lenkei, T. Pons, N. Lequeux, Sulfobetaine–Vinylimidazole block copolymers: a robust quantum dot surface chemistry expanding bioimaging's horizons. *ACS Nano* **9**, 11479–11489 (2015).

90. C. E. Bass, B. R. Martin, Time course for the induction and maintenance of tolerance to Δ9-tetrahydrocannabinol in mice. *Drug Alcohol Depend.* **60**, 113–119 (2000).
91. D. L. McKinney, M. P. Cassidy, L. M. Collier, B. R. Martin, J. L. Wiley, D. E. Selley, L. J. Sim-Selley, Dose-related differences in the regional pattern of cannabinoid receptor adaptation and in vivo tolerance development to Δ 9 -tetrahydrocannabinol. *J. Pharmacol. Exp. Ther.* **324**, 664–673 (2008).

Acknowledgments: We are grateful to E. Tischler, B. Pintér, E. Horváth, P. Aradi, B. Kókay, and J. K. Leffel for technical support. We also appreciate the support of the Nikon Microscopy Center at the Institute of Experimental Medicine, Nikon Europe B.V., Nikon Austria GmbH, and Auro-Science Consulting. We thank D. Dimen, C. Shumaker, J. Brunner, N. Holderith, Z. Nusser, V. Oláh, S. Prokop, and J. Szabadics for valuable discussions and comments; K. Mackie for help in THC experiments and critical comments on the manuscript; and L. Cruchet, T. Pons, and N. Lequeux for help with single-molecule tracking, QD synthesis, and surface modification. We are grateful to B. Cravatt, K. Sakimura, and A. Zimmer for providing KO mice. I.K. holds the Naus Family Chair in Addiction Sciences in the Department of Psychological and Brain Sciences at Indiana University Bloomington. **Funding:** This work was funded by the following: National Research, Development and Innovation Office, Hungary VEKOP-2.3.3-15-2016-00013 (I.K.); Frontier Program KKP129961 (I.K.); National Institutes of Health grant R01NS099457 (I.S., I.K.); National Institutes of Health grant P30DA056410 (I.K.); National Institutes of Health grant R01DA044925 (I.K.); National Institutes of Health grant NS131728 (I.S.); McNair Medical Institute at The Robert and Janice McNair Foundation (B.D.); National Institute of Neurological Disorders and Stroke grant R00NS117795 (B.D.); New National Excellence Program of the Ministry for Innovation and Technology ÚNKP-19-3-III-SE-16 (B.B.); University of Cagliari RICCAR 2017 (M.M.); European Molecular Biology Organization ASTF 371-2016 (C.S.); PSL Nanopaint grant from PSL Research University (D.Z.); ECOS Sud Program PA20N03 (D.Z., M.T.); Argentinean Ministry of Science, Technology and Innovation PICT 2020-SerieA-01312 (M.T.); Ministry of Culture and Innovation of Hungary from the National Research, Development and Innovation Fund TKP2021-EGA (B.T.); and National Laboratory of Translational Neuroscience support by the Recovery and Resilience Facility of the European Union within the framework of Program Széchenyi Plan Plus RRF-2.3.1-21-2022-00011 (I.K.). **Author contributions:** Conceptualization: B.B., B.D., K.K., D.Z., M.T., L.B., Z.L., I.S., and I.K. Data curation: B.B. Formal analysis: B.B., B.D., K.K., M.Z., V.M., G.Y.B., D.Z., M.K., and Z.L. Funding acquisition: B.B., M.T., I.S., and I.K. Investigation: B.B., K.K., M.Z., V.M., G.Y.B., D.Z., M.T., C.S., M.K., and B.T. Methodology: B.B., B.D., K.K., V.M., D.Z., M.K., M.L., Z.L., and I.S. Project administration: M.T., Z.L., I.S., and I.K. Resources: M.T., C.S., B.T., and M.M. Software: B.D., M.Z., and L.B. Supervision: M.T., L.B., I.S., and I.K. Validation: K.K., M.Z., M.T., and Z.L. Visualization: B.B., K.K., G.Y.B., D.Z., M.T., and I.S. Writing—original draft: B.B., B.D., K.K., M.T., Z.L., and I.K. Writing—review and editing: B.B., B.D., V.M., G.Y.B., M.T., M.K., M.L., E.S.V., M.M., L.B., Z.L., I.S., and I.K. **Competing interests:** I.S. declares unrelated consultant activity for Actio Biosciences, CODA Biotherapeutics, MapLight Therapeutics, Praxis Precision Medicines, and Ray Therapeutics. The other authors declare that they have no competing interests. **Data and materials availability:** All data needed to evaluate the conclusions in the paper are present in the paper and/or the Supplementary Materials.

Submitted 11 January 2024
Accepted 23 April 2024
Published 29 May 2024
10.1126/sciadv.ado0077